Title
K2P2.1 (TREK-1)-Activator Complexes Reveal a Cryptic Selectivity Filter Binding Site

Journal
Biophysical Journal, 114(3)

ISSN
0006-3495

Authors
Lolicato, Marco
Arrigoni, Cristina
Mori, Takahiro
et al.

Publication Date
2018-02-01

DOI
10.1016/j.bpj.2017.11.1725

Peer reviewed

LETTER

doi:10.1038/nature22988

K_{2P}2.1 (TREK-1)–activator complexes reveal a cryptic selectivity filter binding site

Marco Lolicato[1], Cristina Arrigoni[1], Takahiro Mori[2], Yoko Sekioka[2], Clifford Bryant[3], Kimberly A. Clark[1] & Daniel L. Minor Jr[1,4,5,6,7]

Polymodal thermo- and mechanosensitive two-pore domain potassium (K_{2P}) channels of the TREK[1] subfamily generate 'leak' currents that regulate neuronal excitability, respond to lipids, temperature and mechanical stretch, and influence pain, temperature perception and anaesthetic responses[1–3]. These dimeric voltage-gated ion channel (VGIC) superfamily members have a unique topology comprising two pore-forming regions per subunit[4–6]. In contrast to other potassium channels, K_{2P} channels use a selectivity filter 'C-type' gate[7–10] as the principal gating site. Despite recent advances[3,11,12], poor pharmacological profiles of K_{2P} channels limit mechanistic and biological studies. Here we describe a class of small-molecule TREK activators that directly stimulate the C-type gate by acting as molecular wedges that restrict interdomain interface movement behind the selectivity filter. Structures of K_{2P}2.1 (also known as TREK-1) alone and with two selective K_{2P}2.1 (TREK-1) and K_{2P}10.1 (TREK-2) activators—an *N*-aryl-sulfonamide, ML335, and a thiophene-carboxamide, ML402—define a cryptic binding pocket unlike other ion channel small-molecule binding sites and, together with functional studies, identify a cation–π interaction that controls selectivity. Together, our data reveal a druggable K_{2P} site that stabilizes the C-type gate 'leak mode' and provide direct evidence for K_{2P} selectivity filter gating.

$K_{2P}2.1_{cryst}$ (that is, the construct used for crystallization studies, see Methods for full description; Extended Data Fig. 1a, b) crystallized alone and with activators ML335 (*N*-[(2,4-dichlorophenyl) methyl]-4-(methanesulfonamido) benzamide) and ML402 (*N*-[2-(4-chloro-2-methylphenoxy)ethyl]thiophene-2-carboxamide) diffracted X-rays to 3.1 Å, 3.0 Å and 2.8 Å, respectively (Extended Data Table 1) enabling structure determination (Extended Data Fig. 1c). $K_{2P}2.1_{cryst}$ has a domain-swapped M1 helix, extracellular CAP domain, and an unimpeded aqueous path between the intracellular side and selectivity filter, similar to prior TREK subfamily structures[6,13–15] (Fig. 1a). Features absent in prior K_{2P} structures include a C-terminal tail (C-tail) that is five helical turns longer than in K_{2P}10.1[6], Trp295–Val321 (Fig. 1a, Extended Data Fig. 1c), the 111–128 loop connecting the P1 pore helix and CAP bearing the extracellular pH sensor, His126 (refs 16, 17) (Fig. 1a, Extended Data Fig. 1d), and a set of bound lipids (Extended Data Fig. 1e, f).

Structures of the ML335 and ML402 complexes revealed unambiguous density for two activators per channel (Fig. 1b, Extended Data Fig. 2a–e) occupying an L-shaped pocket behind the selectivity filter formed by the P1 pore helix and M4 transmembrane helix intrasubunit interface (Fig. 1c, d). Notably, and in contrast to the activated mutant $K_{2P}2.1(G137I)$[7], $K_{2P}2.1_{cryst}$ responds to both ML335 and ML402 (Extended Data Fig. 2f–i). The ML335/ML402 binding pocket differs from the TREK antagonist norfluoxetine[6] binding site (Fig. 1e) and is dissimilar to other VGIC superfamily pore domain antagonist sites[18,19] (Extended Data Fig. 3). Thus, the ML335/ML402 site, dubbed the 'K_{2P} modulator pocket', establishes a novel point for VGIC superfamily small molecule modulation.

The K_{2P} modulator pocket comprises a 'P1 face' and an 'M4 face' that form a common set of hydrogen bonds, π–π, and cation–π[20] interactions with ML335 and ML402 (Fig. 2a, b and Extended Data Fig. 4a, b). Both compounds adopt an L-shaped conformation enabling their 'upper ring' (ML335 *N*-aryl sulfonamide and ML402 thiophene) and 'lower ring' (ML335 dicholoro-benzyl and ML402 aryl ether) to engage the P1 helix residue Phe134 through face–face and edge–face interactions, respectively (Fig. 2a, b). On the M4 face, the upper and lower rings make a cation–π interaction with Lys271 and edge–face interaction with Trp275, respectively (Fig. 2, Extended Data Figs 2a, b and 4a, b). The amide groups of both compounds also make hydrogen bonds with the Ala259 carbonyl on the loop connecting the second selectivity filter. The ML335 sulfonamide forms additional interactions with the Gly260 carbonyl on the same loop, the P1 face Ser131 hydroxyl, the 111–128 loop His126 imidazole nitrogen, and Asn147 on the first selectivity filter (Fig. 2a, Extended Data Fig. 4a).

The K_{2P} modulator pocket constitutes a cryptic binding site requiring conformational changes centred around Phe134, Lys271 and Trp275 (Fig. 2c, d, Supplementary Video 1). Without activators, Phe134 and the M4 helix N-terminal end occlude the pocket. These elements move towards the selectivity filter and away from the P1 helix, respectively, to allow access. Lys271 and Trp275 are mobile in the unliganded structure (Extended Data Figs 5a and 6b), change conformation to form modulator interactions, and together with Phe134 have reduced bound state mobility (Extended Data Fig. 5a–c, and Extended Data Table 2a). Hence, both compounds act as wedges driven into the selectivity filter supporting structure, a mode reminiscent of other channel modulators[21,22]. Notably, the K_{2P} modulator pocket includes gain-of-function mutation sites, Gly137 and Trp275, affecting all TREK subfamily members[7,8,15,23] (Extended Data Fig. 6b). Together, these observations indicate that the P1–M4 interface is a hub for conformational changes causing TREK subfamily activation and that P1–M4 interface stabilization is central to ML335 and ML402 action.

K_{2P} activator pocket residues that contact the compounds are identical among TREK subfamily members, except for the Lys271 cation–π interaction, and diverge in other K_{2P} subtypes (Extended Data Fig. 4c, d). Comparison with K_{2P}10.1[6] and K_{2P}4.1 (TRAAK)[4,13–15] (Extended Data Fig. 6a, Extended Data Table 2b) reveals no selectivity filter conformation differences. This structural similarity supports the idea that ML335 and ML402 influence selectivity filter dynamics, similar to inferences from structural studies of P1–M4 interface gain-of-function mutants[15]. There are notable differences in the first two M4 helical turns of the K_{2P} modulator pocket and the conformations of the Phe134 and Trp275 equivalent positions among TREK subfamily structures (Extended Data Fig. 6b–f).

[1]Cardiovascular Research Institute, University of California, San Francisco, California 941158-9001, USA. [2]Ono Pharmaceutical Co. Ltd, Mishima-Gun, Osaka 618-8585, Japan. [3]Small Molecule Discovery Center, University of California, San Francisco, California 93858-2330, USA. [4]Departments of Biochemistry and Biophysics, and Cellular and Molecular Pharmacology, University of California, San Francisco, California 941158-9001, USA. [5]California Institute for Quantitative Biomedical Research, University of California, San Francisco, California 941158-9001, USA. [6]Kavli Institute for Fundamental Neuroscience, University of California, San Francisco, California 941158-9001, USA. [7]Molecular Biophysics and Integrated Bio-imaging Division, Lawrence Berkeley National Laboratory, Berkeley, California 94720, USA.

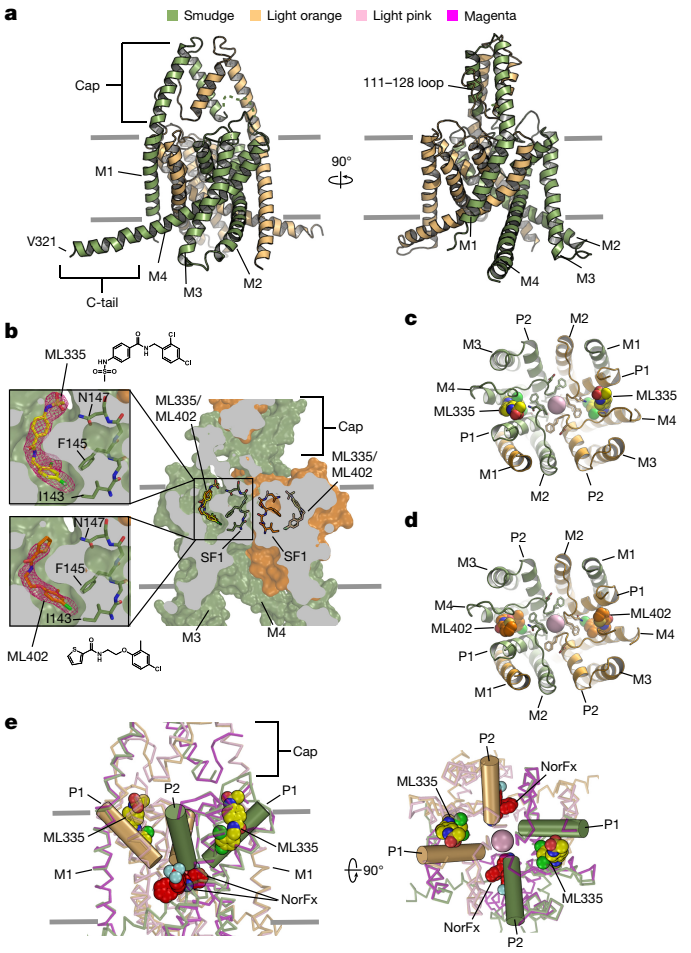

Figure 1 | $K_{2P}2.1$ structures. a, $K_{2P}2.1_{cryst}$ cartoon (smudge and light orange, colours defined according to PyMol) smudge subunit extracellular cap domain (Cap), M1–M4 transmembrane helices, C-tail, and V321 are labelled. **b**, K_{2P} modulator pocket cutaway. Cut-outs display ML335 and ML402 $F_o - F_c$ densities (3.0σ). ML335, ML402 and selectivity filter 1 (SF1) are sticks. **c**, **d**, Extracellular views excluding the cap domain of ML335 (**c**) and ML402 (**d**) binding sites. ML335 and ML402 are space filling. Selectivity filter sidechains are sticks. **e**, Wire representation comparing $K_{2P}2.1$–ML335 (smudge and light orange) and $K_{2P}10.1$–norfluoxetine[6] (light pink and magenta) binding sites. $K_{2P}2.1$ P1 and P2 are cylinders. ML335 (yellow) and norfluoxetine (NorFx; red) are space filling. In all panels select residues and channel elements are indicated, and where present, grey lines indicate the membrane.

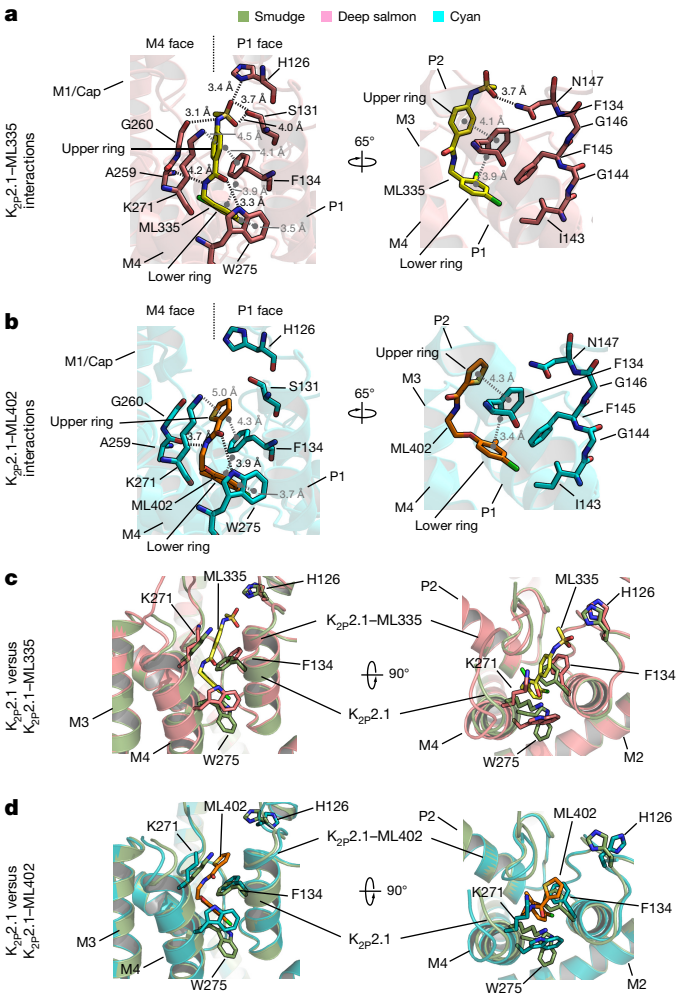

Figure 2 | $K_{2P}2.1$–activator interactions. a, **b**, Cartoon diagram of $K_{2P}2.1$–ML335 (**a**) and $K_{2P}2.1$–ML402 (**b**) interactions. Electrostatic and hydrogen bond interactions are black. Cation–π and π–π interactions are grey. **c**, **d**, Comparison of $K_{2P}2.1$ (smudge) with $K_{2P}2.1$–ML335 (pink; **c**) and $K_{2P}2.1$–ML402 (cyan; **d**).

Given the varied conformations of these residues in the absence of activators and mobility changes between the unliganded and liganded structures (Extended Data Fig. 5), the main action of the activators appears to be to limit the conformations sampled by P1–M4 interface elements.

The $K_{2P}2.1$ C-tail senses phospholipid[24,25], phosphorylation[26,27], temperature[7,28], and pressure[27] gating commands and forms a continuous helix with M4 (Fig. 3a). Prior TREK subfamily structures uncovered varied M4 conformations spanning extremes termed 'up' and 'down'[4,6,13–15]. Proposals that the up[14], down[15], or both conformations are active[6,23], have been advanced. In all $K_{2P}2.1$structures, M4 is up (Fig. 1a) and the selectivity filter sites S1–S4 are occupied by potassium ions (Extended Data Fig. 6a). Because both C-tails make lattice contacts (Extended Data Fig. 1g) that can influence M4[13,15], the $K_{2P}2.1$ structures presented here cannot directly address the controversy regarding M4 status. Nevertheless, the activator-bound selectivity filter is compatible with the up M4 conformation.

The C-tail has two faces, an electropositive patch comprising four residues implicated in PIP_2 modulation (Arg297, Lys301, Lys302 and Lys304)[24,25], and a face housing the intracellular proton sensor site, Glu306[29], and inhibitory phosphorylation site, Ser300[26] (Fig. 3a, b). The channel electrostatic profile shows a second positively charged region at the M1–M2–M4 junction (Fig. 3b) suggesting that the resultant inter-helical groove may be a phospholipid binding site.

All three $K_{2P}2.1$ structures revealed tubular densities at locations different from previous K_{2P} lipid binding sites[4,6,14,15], denoted as lipids L1, L2, and L3 (Fig. 3c, Extended Data Fig. 1e, f). L1 resides at the M2–P2 inter-subunit junction (Fig. 3c). L2 and L3 are part of a single phospholipid (Extended Data Fig. 1e, f) and sit in the groove formed by the positively charged M1–M2–M4 inter-subunit junction (Fig. 3b, c and Extended Data Fig. 1e, f). The L2–L3 site seems to be a prime point for modulatory lipids, as the positively charged residues that affect PIP_2 responses[24,25] are on the helical face opposite to L2–L3, and M4 conformational changes could affect how these residues interact with regulatory lipid head-groups.

Xenopus oocyte two-electrode voltage-clamp measurements show that ML335 and ML402 activate $K_{2P}2.1$and $K_{2P}10.1$ but not $K_{2P}4.1$ ($14.3 \pm 2.7\,\mu M$, $K_{2P}2.1$–ML335; $13.7 \pm 7.0\,\mu M$, $K_{2P}2.1$–ML402; $5.2 \pm 0.5\,\mu M$, $K_{2P}10.1$–ML335; and $5.9 \pm 1.6\,\mu M$, $K_{2P}10.1$–ML402) (Fig. 4a–f and Extended Data Fig. 7a–c). The K_{2P} modulator pocket has a single difference among TREK subfamily members at the cation–π interaction position, $K_{2P}2.1$ Lys271 (Extended Data Fig. 4c), which is also a lysine in $K_{2P}10.1$ but a glutamine in $K_{2P}4.1$. Hence, we

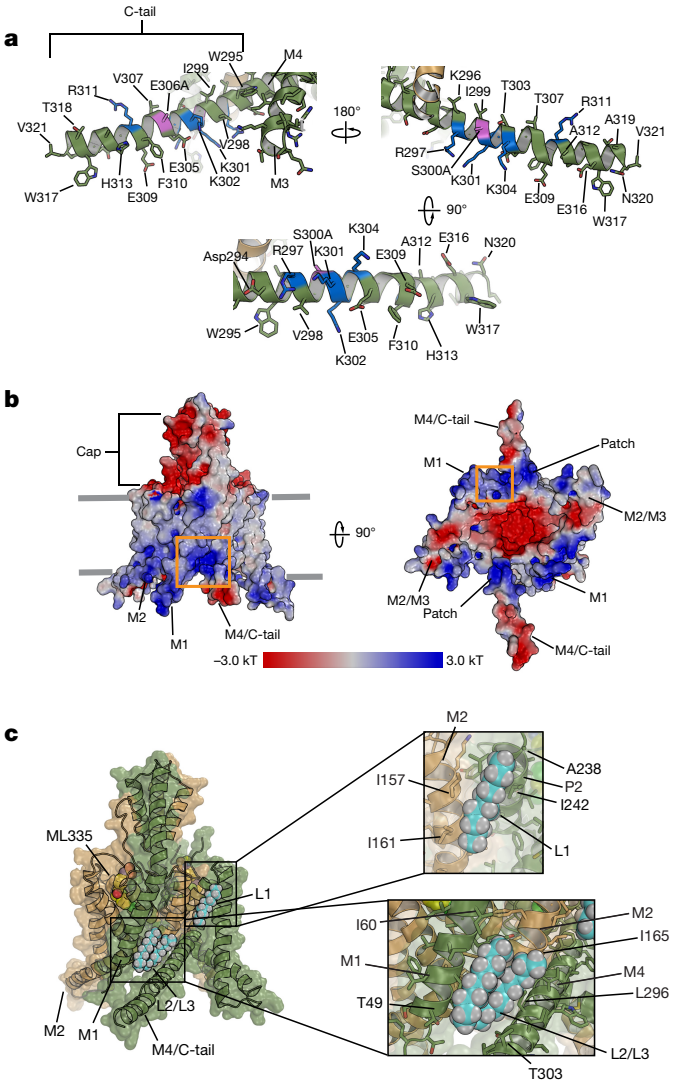

Figure 3 | $K_{2P}2.1$ C-tail and lipid binding sites. a, $K_{2P}2.1$ C-tail. Positively charged residues are blue. S300A and E306A, a site having slight distortion from helical geometry, are magenta. **b**, $K_{2P}2.1$ Electrostatic surface potential. Orange box highlights M1–M2–M4 junction. Cytoplasmic view (right) indicates C-tail positively charged patch. **c**, Lipids L1, L2 and L3 (cyan and white) shown as space filling. ML335 (yellow) is indicated. Insets show lipid binding pocket details.

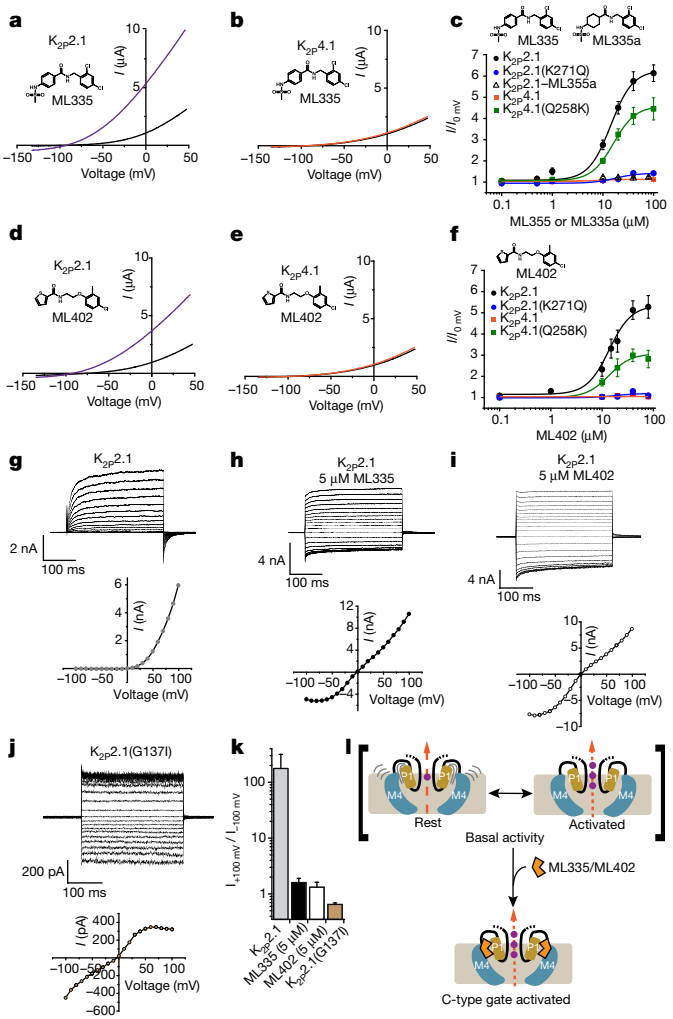

Figure 4 | $K_{2P}2.1$ activator function. a, **b**, Exemplar current traces for $K_{2P}2.1$ (black) with 20 μM ML335 (purple) (**a**) and $K_{2P}4.1$ (black) with 50 μM ML335 (orange) (**b**). **c**, ML335 dose–response curves for $K_{2P}2.1$ (black), $EC_{50} = 14.3 \pm 2.7$ μM ($n \geq 5$); $K_{2P}2.1$(K271Q) (blue filled circles); $K_{2P}4.1$ (orange); and $K_{2P}4.1$(Q258K) (green), $EC_{50} = 16.2 \pm 3.0$ μM ($n \geq 4$); and $K_{2P}2.1$–ML335a (black open triangles). **d**, **e**, Exemplar current traces for $K_{2P}2.1$ (black) with 20 μM ML402 (purple) (**d**) and $K_{2P}4.1$ (black) with 50 μM ML335 (orange) (**e**). **f**, ML402 dose–response curves for $K_{2P}2.1$ (black), $EC_{50} = 13.7 \pm 7.0$ μM ($n \geq 3$); $K_{2P}2.1$(K271Q) (blue); $K_{2P}2.1$ (blue); $K_{2P}4.1$ (orange); and $K_{2P}4.1$(Q258K) (green), $EC_{50} = 13.6 \pm 1.5$ μM ($n \geq 3$). **g**–**j**, Exemplar current traces and voltage–current relationships for indicated K_{2P} channels in HEK293 inside-out patches in 150 mM $K^+_{[out]}$/150 mM $Rb^+_{[in]}$ for $K_{2P}2.1$ (**g**), $K_{2P}2.1$ with 5 μM ML335 (**h**), $K_{2P}2.1$ with 5 μM ML402 (**i**), and $K_{2P}2.1$(G137I) (**j**). **k**, Rectification coefficients ($I_{+100\,mV}/I_{-100\,mV}$) from recordings ($n \geq 3$) made in **g**–**j**. **l**, TREK activation model. Grey lines indicate mobile P1 (tan) and M4 (blue). C-type activators (orange) stabilize the selectivity filter and channel 'leak mode'. Potassium ions are purple. Gap in arrows indicates current flow intensity. Membrane is grey.

asked whether this residue controlled the selective actions of ML335 and ML402. Swapping the Lys271 equivalent between $K_{2P}2.1$ and $K_{2P}4.1$ resulted in a clear phenotype reversal for ML335 and M402 activation (Fig. 4c and f, Extended Data Fig. 7d-g). $K_{2P}2.1$(K271Q) was insensitive to ML335 and ML402, whereas $K_{2P}4.1$(Q258K) responded to both with a similar EC_{50} to $K_{2P}2.1$(14.3 ± 2.7 μM, $K_{2P}2.1$–ML335; 16.2 ± 3.0 μM, $K_{2P}4.1$(Q258K)–ML335; 13.7 ± 7.0 μM, $K_{2P}2.1$–ML402; 13.6 ± 1.5 μM, $K_{2P}4.1$(Q258K)–ML402) but with a lower magnitude response than $K_{2P}2.1$. Notably, the effects of TREK subfamily activators arachidonic acid[27,30], BL-1249[31,32], and ML67-33[11] were unchanged (Extended Data Fig. 7h–k). To probe the cation–π interaction further, we synthesized a ML335 congener, ML335a, in which the aromatic upper ring was replaced with an aliphatic ring (Fig. 4c). ML335a had no effect on $K_{2P}2.1$ (Fig. 4c), supporting the importance of the cation–π interaction. Together, these data identify the Lys271 cation–π interaction as the origin of ML335/ML402 subtype selectivity and establish that this interaction is essential for activation.

The principal K_{2P} channel gating site is the selectivity filter C-type gate[7–10]. This gate is highly sensitive to permeant ions[8,16,17] and is thought to function via 'flux gating' whereby outward, but not inward, ion flow stabilizes the active conformation[9]. Physiological $K_{2P}2.1$ activators, such as arachidonic acid, PIP_2, and intracellular acidification, shift the channel from outward rectifier mode to an ohmic 'leak mode'[9]. Because the K_{2P} modulator pocket contains architectural elements that support the activator selectivity and gain-of-function mutants that activate the C-type gate[7,8,15], we asked whether structural changes to the P1–M4 interface caused by ML335, ML402, or gain-of-function mutations affect C-type gate function.

Measurement of $K_{2P}2.1$ in inside-out patches under conditions that potentiate flux-dependent C-type gate activation (150 mM $K^+_{[out]}$ versus 150 mM $Rb^+_{[in]}$)[9] showed the expected outward rectification (Fig. 4g, k).

ML335 and ML402 activate $K_{2P}2.1$ in HEK293 cells similar to their effects in *Xenopus* oocytes ($5.2 \pm 0.8\,\mu M$ and $5.9 \pm 1.6\,\mu M$ for ML335 and ML402, respectively ($n \geq 3$)) (Fig. 4g–i and Extended Data Fig. 8a). Compound application essentially eliminated flux-dependent outward rectification (Fig. 4h, i, k) yielding a rectification coefficient ($I_{+100\,mV}/I_{-100\,mV}$) of approximately 1. This outcome matches physiological activator effects[9] and establishes that ML335 and ML402 activate the C-type gate. The $K_{2P}4.1$ gain-of-function mutation G124I reshapes the K_{2P} modulator pocket through structural consequences similar to ML335/ML402, namely an outward M4 movement and repositioning of the $K_{2P}2.1$ Phe134 equivalent residue[15] (Extended Data Fig. 6f). $K_{2P}2.1$(G137I) and $K_{2P}4.1$(G124I)[7,15] caused a similar mode shift and rectification coefficient change to ML335 and ML402 (Fig. 4j, k and Extended Data Fig. 8b–d) establishing that K_{2P} modulator pocket manipulation by ML335/ML402 binding or mutation directly activates the selectivity filter C-type gate. Together with the compound-binding-induced mobility reduction of the P1–M4 interface (Extended Data Fig. 5) and lack of K_{2P} selectivity filter structural differences (Extended Data Fig. 6a), our findings strongly support the idea that direct C-type gate activators stimulate function by reducing the dynamics of the selectivity filter and surrounding structure.

The roles of TREK channels in ischaemia, pain, analgesia and anaesthetic responses[1] suggest that TREK activators could provide new avenues for neuroprotection and pain control. Many natural TREK regulators are thought to act on the C-tail[7,24–29] and influence the C-type gate through M4[6–8,15,23], the movement of which is targeted by the antagonist norfluoextine[6,23]. In this regard, ML335 and ML402 represent a new K_{2P} modulator class, as they function by binding directly to a pocket at the heart of the channel active site, the C-type gate, rather than influencing the C-tail or M4.

The K_{2P} modulator pocket defines the first VGIC superfamily pore domain small-molecule activator site and differs from antagonist sites occupying lateral fenestrations below the selectivity filter[6,18] (Fig. 1e and Extended Data Fig. 3a). Voltage-gated calcium channel antagonists, amlodipine and nifedipine[19], act at an interface similar to the K_{2P} modulator pocket, but at a pore domain outer rim site normally occupied by lipids[19] (Extended Data Fig. 3b). Notably, all of these small-molecule sites are found at interfaces that are thought to move during gating[6,18,19], highlighting the potential of channel inter-subunit interfaces as small-molecule control sites.

Our findings provide a structural basis for understanding K_{2P} C-type gate activation. The K_{2P} modulator pocket in unliganded $K_{2P}2.1$ displays mobility in key elements that is reduced upon activator engagement (Fig. 4l, Extended Data Figs 5, 6b–d and Supplementary Video 1). Notably, the K_{2P} modulator pocket M4 helix N-terminal end, an important site for channel activation[8] and conduit for transmitting C-tail sensor domain cues to the C-type gate[7,8], adopts a similar position in the ML335 and ML402 $K_{2P}2.1$ complexes and in $K_{2P}4.1$(G124I) (Extended Data Fig. 6f). As the remainder of M4 is 'up' for the $K_{2P}2.1$ activator complexes, but 'down' for $K_{2P}4.1$(G124I), the data support the idea that M4 position is not the sole determinant of channel state[23]. The importance of changes in P1–M4 interface dynamics explain how M4 can affect channel function and allow the up or down conformations to activate the channel[23], as both states could limit the mobility of the P1/M4 interface. Such plasticity may be important for enabling TREK subfamily polymodal modulation. Our findings indicate that under basal conditions, $K_{2P}2.1$ equilibrates between a resting state having a mobile P1–M4 interface and an activated state in which the mobility of this site is limited. ML335 and ML402 directly stabilize the C-type gate by acting like molecular wedges that reduce P1–M4 interface dynamics (Fig. 4l, Extended Data Fig. 5 and Extended Data Table 2a) and cause the filter to enter the leak mode (Fig. 4h, i), bypassing modulation mechanisms that may involve other channel regions. The K_{2P} modulator pocket properties revealed by our studies raise the possibility that natural processes or native signalling molecules may also target this site.

Opening the cryptic K_{2P} modulator pocket requires small movements of few residues, similar to soluble protein cryptic modulator sites[33]. K_{2P} modulator pocket diversity (Extended Data Fig. 4c, d), the P1–M4 interface susceptibility to gain-of-function mutations[7,8], and demonstration that a single residue therein can define modulator selectivity suggests that this site may be amenable for K_{2P} subtype-selective pharmacology development. As the fundamental pocket architecture is conserved in the VGIC superfamily, similar modulatory mechanisms may exist in other superfamily members where selectivity-filter-based gating is central. Thus, this site should provide a fertile target for channel modulator discovery.

Online Content Methods, along with any additional Extended Data display items and Source Data, are available in the online version of the paper; references unique to these sections appear only in the online paper.

Received 17 January; accepted 12 May 2017.
Published online 10 July 2017.

1. Feliciangeli, S., Chatelain, F. C., Bichet, D. & Lesage, F. The family of K2P channels: salient structural and functional properties. *J. Physiol. (Lond.)* **593,** 2587–2603 (2015).
2. Devilliers, M. *et al.* Activation of TREK-1 by morphine results in analgesia without adverse side effects. *Nat. Commun.* **4,** 2941 (2013).
3. Vivier, D. *et al.* Development of the first two-pore domain potassium channel TWIK-related K^+ channel 1-selective agonist possessing *in vivo* anti-nociceptive activity. *J. Med. Chem.* **60,** 1076–1088 (2017).
4. Brohawn, S. G., del Mármol, J. & MacKinnon, R. Crystal structure of the human K2P TRAAK, a lipid- and mechano-sensitive K^+ ion channel. *Science* **335,** 436–441 (2012).
5. Miller, A. N. & Long, S. B. Crystal structure of the human two-pore domain potassium channel K2P1. *Science* **335,** 432–436 (2012).
6. Dong, Y. Y. *et al.* K2P channel gating mechanisms revealed by structures of TREK-2 and a complex with Prozac. *Science* **347,** 1256–1259 (2015).
7. Bagriantsev, S. N., Clark, K. A. & Minor, D. L., Jr. Metabolic and thermal stimuli control K(2P)2.1 (TREK-1) through modular sensory and gating domains. *EMBO J.* **31,** 3297–3308 (2012).
8. Bagriantsev, S. N., Peyronnet, R., Clark, K. A., Honoré, E. & Minor, D. L., Jr. Multiple modalities converge on a common gate to control K2P channel function. *EMBO J.* **30,** 3594–3606 (2011).
9. Schewe, M. *et al.* A non-canonical voltage-sensing mechanism controls gating in K2P K^+ channels. *Cell* **164,** 937–949 (2016).
10. Piechotta, P. L. *et al.* The pore structure and gating mechanism of K2P channels. *EMBO J.* **30,** 3607–3619 (2011).
11. Bagriantsev, S. N. *et al.* A high-throughput functional screen identifies small molecule regulators of temperature- and mechano-sensitive K2P channels. *ACS Chem. Biol.* **8,** 1841–1851 (2013).
12. Su, Z., Brown, E. C., Wang, W. & MacKinnon, R. Novel cell-free high-throughput screening method for pharmacological tools targeting K_+ channels. *Proc. Natl Acad. Sci. USA* **113,** 5748–5753 (2016).
13. Brohawn, S. G., Campbell, E. B. & MacKinnon, R. Domain-swapped chain connectivity and gated membrane access in a Fab-mediated crystal of the human TRAAK K_+ channel. *Proc. Natl Acad. Sci. USA* **110,** 2129–2134 (2013).
14. Brohawn, S. G., Campbell, E. B. & MacKinnon, R. Physical mechanism for gating and mechanosensitivity of the human TRAAK K_+ channel. *Nature* **516,** 126–130 (2014).
15. Lolicato, M., Riegelhaupt, P. M., Arrigoni, C., Clark, K. A. & Minor, D. L., Jr Transmembrane helix straightening and buckling underlies activation of mechanosensitive and thermosensitive K_{2P} channels. *Neuron* **84,** 1198–1212 (2014).
16. Cohen, A., Ben-Abu, Y., Hen, S. & Zilberberg, N. A novel mechanism for human K2P2.1 channel gating. Facilitation of C-type gating by protonation of extracellular histidine residues. *J. Biol. Chem.* **283,** 19448–19455 (2008).
17. Sandoz, G., Douguet, D., Chatelain, F., Lazdunski, M. & Lesage, F. Extracellular acidification exerts opposite actions on TREK1 and TREK2 potassium channels via a single conserved histidine residue. *Proc. Natl Acad. Sci. USA* **106,** 14628–14633 (2009).
18. Bagnéris, C. *et al.* Prokaryotic NavMs channel as a structural and functional model for eukaryotic sodium channel antagonism. *Proc. Natl Acad. Sci. USA* **111,** 8428–8433 (2014).
19. Tang, L. *et al.* Structural basis for inhibition of a voltage-gated Ca^{2+} channel by $Ca^{(2+)}$ antagonist drugs. *Nature* **537,** 117–121 (2016).
20. Kearney, P. C. *et al.* Molecular recognition in aqueous-media – new binding-studies provide further insights into the cation-pi interaction and related phenomena. *J. Am. Chem. Soc.* **115,** 9907–9919 (1993).
21. Hibbs, R. E. & Gouaux, E. Principles of activation and permeation in an anion-selective Cys-loop receptor. *Nature* **474,** 54–60 (2011).
22. Yelshanskaya, M. V. *et al.* Structural bases of noncompetitive inhibition of AMPA-subtype ionotropic glutamate receptors by antiepileptic drugs. *Neuron* **91,** 1305–1315 (2016).
23. McClenaghan, C. *et al.* Polymodal activation of the TREK-2 K_{2P} channel produces structurally distinct open states. *J. Gen. Physiol.* **147,** 497–505 (2016).

24. Chemin, J. *et al.* A phospholipid sensor controls mechanogating of the K^+ channel TREK-1. *EMBO J.* **24,** 44–53 (2005).
25. Chemin, J. *et al.* Up- and down-regulation of the mechano-gated K(2P) channel TREK-1 by PIP (2) and other membrane phospholipids. *Pflugers Arch.* **455,** 97–103 (2007).
26. Murbartián, J., Lei, Q., Sando, J. J. & Bayliss, D. A. Sequential phosphorylation mediates receptor- and kinase-induced inhibition of TREK-1 background potassium channels. *J. Biol. Chem.* **280,** 30175–30184 (2005).
27. Patel, A. J. *et al.* A mammalian two pore domain mechano-gated S-like K^+ channel. *EMBO J.* **17,** 4283–4290 (1998).
28. Maingret, F. *et al.* TREK-1 is a heat-activated background K^+ channel. *EMBO J.* **19,** 2483–2491 (2000).
29. Honoré, E., Maingret, F., Lazdunski, M. & Patel, A. J. An intracellular proton sensor commands lipid- and mechano-gating of the K^+ channel TREK-1. *EMBO J.* **21,** 2968–2976 (2002).
30. Fink, M. *et al.* Cloning, functional expression and brain localization of a novel unconventional outward rectifier K^+ channel. *EMBO J.* **15,** 6854–6862 (1996).
31. Veale, E. L. *et al.* Influence of the N terminus on the biophysical properties and pharmacology of TREK1 potassium channels. *Mol. Pharmacol.* **85,** 671–681 (2014).
32. Tertyshnikova, S. *et al.* BL-1249 [(5,6,7,8-tetrahydro-naphthalen-1-yl)-[2-(1H-tetrazol-5-yl)-phenyl]-amine]: a putative potassium channel opener with bladder-relaxant properties. *J. Pharmacol. Exp. Ther.* **313,** 250–259 (2005).
33. Hardy, J. A. & Wells, J. A. Searching for new allosteric sites in enzymes. *Curr. Opin. Struct. Biol.* **14,** 706–715 (2004).

Supplementary Information is available in the online version of the paper.

Acknowledgements We thank K.Brejc, S. Capponi, M.Grabe and L. Jan for comments, and A. Renslo for comments and synthesis advice. This work was supported by grants R01-MH093603 to D.L.M., and to M.L. and C.A. from the American Heart Association.

Author Contributions M.L., C.A., C.B. and D.L.M. conceived the study and designed the experiments. T.M. and Y.S. conceived and ran thallium flux assays. M.L. and C.A. performed experiments. M.L. and K.A.C. expressed and purified proteins. M.L. performed crystallization and structure determination. M.L. and C.A. performed electrophysiological experiments and analysed the data. C.B. designed synthetic routes, synthesized, and purified the compounds. D.L.M analysed data and provided guidance and support. M.L., C.A. and D.L.M. wrote the paper.

Author Information Reprints and permissions information is available at www.nature.com/reprints. The authors declare competing financial interests: details are available in the online version of the paper. Readers are welcome to comment on the online version of the paper. Publisher's note: Springer Nature remains neutral with regard to jurisdictional claims in published maps and institutional affiliations. Correspondence and requests for materials should be addressed to D.L.M. (daniel.minor@ucsf.edu).

Reviewer Information *Nature* thanks E. Honoré and the other anonymous reviewer(s) for their contribution to the peer review of this work.

METHODS

No statistical methods were used to predetermine sample size. No randomization or blinding was used.

Construct screening. A set of mutants and deletion constructs of mouse $K_{2P}2.1$[1] bearing a C-terminal TEV protease cleavage site and GFP were expressed from a pcDNA3.1 in HEK293 cells and screened for expression level and peak quality using fluorescence-detection size-exclusion chromatography (FSEC)[34–36]. These efforts identified a construct, hereafter called $K_{2P}2.1_{cryst}$, encompassing residues 21–322 and bearing the following mutations: K84R, Q85E, T86K, I88L, A89R, Q90A, A92P, N95S, S96D, T97Q, N119A, S300A, E306A. The first nine mutations are located on the surface of the cap domain and greatly increased expression. N119A targets a putative glycosylation site. S300A and E306A are previously studied mutants[7] that improved the biochemical properties of the purified protein. The reduced response of $K_{2P}2.1_{cryst}$ to ML335 and ML402 probably results from partial activation of the channel in a cellular context owing to the incorporation of the E306A mutation[7,29] and is compatible with the model proposed in Fig. 4l in which basal activity is increased by E306A but can nevertheless be shifted to the C-type gate activated state by activator binding and C-type gate stabilization.

Protein expression. $K_{2P}2.1_{cryst}$ bearing a C-terminal green fluorescent protein (GFP) and His_{10} tag was expressed from a previously described *Pichia pastoris* pPICZ vector[4]. Plasmids were linearized with *PmeI* and transformed into *P. pastoris* SMD1163H by electroporation. Multi-integration recombinants were selected by plating transformants onto yeast extract peptone dextrose sorbitol (YPDS) plates having increasing concentrations of zeocin (1–4 mg ml^{-1}). Expression levels of individual transformants were evaluated by FSEC as previously described[15].

Large-scale expression was carried out in a 7L Bioreactor (Labfors5, Infors HT). First, a 250 ml starting culture was grown in buffered minimal medium (2× YNB, 1% glycerol, 0.4 mg l^{-1} biotin, 100 mM potassium phosphate, pH 6.0) in shaker flasks for two days at 29 °C. Cells were pelleted by centrifugation (3,000*g*, 10 minutes, 20 °C) and used to inoculate the bioreactor. Cells were grown in minimal medium (4% glycerol, 0.93 g l^{-1} $CaSO_4{\cdot}2H_2O$, 18.2 g l^{-1} K_2SO_4, 14.9 g l^{-1} $MgSO_4.7H_2O$, 9 g l^{-1} $(NH_4)_2SO_4$, 25 g l^{-1} Na^+ hexametaphosphate, 4.25 ml l^{-1} PTM_1 trace metals stock solution prepared accordingly to standard Invitrogen protocol) until the glycerol in the fermenter was completely metabolized marked by a spike in pO_2 (around 24 h). Fed-batch phase was then initiated by adding a solution of 50% glycerol and 12 ml l^{-1} of trace metals at 15–30% of full pump speed until the wet cell mass reached approximately 250 g l^{-1} (around 24 h). pO_2 was measured continuously and kept at a minimum of 30%. Feed rate was automatically regulated accordingly. pH was maintained at 5.0 by the addition of a 30% ammonium hydroxide solution.

After the fed-batch phase was completed, cells were then starved to deplete glycerol by stopping the feeder pump until a pO_2 spike appeared. After starvation, the temperature was set to 27 °C, and the induction was initiated with addition of methanol in three steps: (1) initially, the methanol concentration was kept at 0.1% for 2 h in order to adapt the cells; (2) methanol concentration was then increased to 0.3% for 3 h; and (3) methanol was then increased to 0.5% and expression continued for 48–60 h. Cells were then pelleted by centrifugation (6,000*g*,1 h, 4 °C), snap frozen in liquid nitrogen, and stored at −80 °C.

Protein purification. In a typical preparation, 50 g of cells were broken by cryo-milling (Retsch model MM400) in liquid nitrogen (5 × 3 min, 25 Hz). All subsequent purification was carried out at 4 °C. Cell powder was added at a ratio of 1 g cell powder to 3 ml lysis buffer (200 mM KCl, 21 mM OGNG (octyl glucose neopentyl glycol, Anatrace), 30 mM HTG (*n*-heptyl-β-D-thioglucopyranoside, Anatrace), 0.1% CHS, 0.1 mg ml^{-1} DNase 1 mM PMSF, 100 mM Tris-Cl, pH 8.2). Membranes were extracted for 3 h with gentle stirring followed by centrifugation (100,000*g*, 45 minutes at 4 °C).

Solubilized proteins were purified by affinity chromatography using batch purification. Anti-GFP nanobodies were conjugated with CNBr Sepharose beads (GE Healthcare, #17-0430-02) according to ref. 37. The resin was added to the cleared supernatant at a ratio of 1 ml of resin per 10 g of cell powder and incubated at 4 °C for 3 h with gentle shaking. Resin was collected into a column and washed with ten column volumes (CV) of buffer A (200 mM KCl, 10 mM OGNG, 15 mM HTG, 0.018% CHS, 50 mM Tris-Cl, pH 8.0) followed by a second wash step using 10 CV of buffer B containing (200 mM KCl, 5 mM OGNG, 15 mM HTG, 0.018% CHS, 50 mM Tris-Cl, pH 8.0). The resin was then washed with additional ten CV of buffer C (200 mM KCl, 3.85 mM OGNG, 15 mM HTG, 0.0156% CHS, 50 mM Tris-Cl, pH 8.0). On column cleavage of the affinity tag was achieved by incubating the resin with buffer C supplemented to contain 350 mM KCl, 1 mM EDTA, and 3C protease[38] at ratio of 50:1 resin volume:protease volume. The resin was incubated overnight at 4 °C. Cleaved sample was collected and the resin washed with two CV of SEC buffer (200 mM KCl, 2.1 mM OGNG, 15 mM HTG, 0.012% CHS, 20 mM Tris-Cl, pH 8.0). Purified sample was concentrated and applied to a Superdex 200 column equilibrated in SEC buffer.

Crystallization and refinement. Purified $K_{2P}2.1_{cryst}$ was concentrated to 6 mg ml^{-1} by centrifugation (Amicon Ultra-15, 50 kDa molecular mass cut-off; Millipore) and crystallized by hanging-drop vapour diffusion at 4 °C using a mixture of 0.2 μl of protein and 0.1 μl of precipitant over 100 μl of reservoir containing 20–25% PEG400, 200 mM KCl, 100 mM HEPES pH 8.0, 1 mM $CdCl_2$. Crystals appeared in 12 h and grew to full size (200–300 μM) in about a week. Crystals were cryo-protected with buffer D (200 mM KCl, 0.2% OGNG, 15 mM HTG, 0.02% CHS, 100 mM HEPES pH 8.0,1 mM $CdCl_2$) with 5% step increase of PEG400 up to a final concentration of 38% and flash-frozen in liquid nitrogen.

$K_{2P}2.1_{cryst}$ ML335 and ML402 complex crystals grew in the same conditions as $K_{2P}2.1_{cryst}$, but the protein was incubated for at least 1 h with 2.5 mM of activator before setting the crystal plates. ML335 and ML402 are insoluble in aqueous solutions, so they were dissolved in 100% DMSO at a concentration of 500 mM. Then each compound was diluted 1:100 in SEC buffer to 5 mM concentration, giving a milky solution. This solution was mixed 1:1 to $K_{2P}2.1_{cryst}$ previously concentrated to 12 mg ml^{-1}. The $K_{2P}2.1_{crys}$ /ML402 mixture resulted in a clear solution, while the mixture with ML335 was slightly milky. The samples were briefly centrifuged in a table-top centrifuge (10,000 *g*) to remove any insoluble material before setting the crystal plates.

Datasets for $K_{2P}2.1$, $K_{2P}2.1$–ML335, and $K_{2P}2.1$–ML402 were collected at 100 K using synchrotron radiation at ALS Beamline 8.3.1 Berkeley, California and APS GM/CAT beamline 23-IDB/D Chicago, Illinois using wavelengths of 1.1159 Å and 1.0332 Å, respectively, processed with XDS[39], scaled and merged with Aimless[40]. Final resolution cut-off was 3.1 Å, 3.0 Å and 2.8 Å for $K_{2P}2.1_{cryst}$, $K_{2P}2.1_{cryst}$–ML335 and $K_{2P}2.1_{cryst}$–ML402, respectively, using the $CC_{1/2}$ criterion[41,42]. Structures were solved by molecular replacement using the $K_{2P}4.1$(G124I) structure (PDB: 4RUE)[15] as search model. Several cycles of manual rebuilding, using COOT[43], and refinement using REFMAC5[44] and PHENIX[45] were carried out to improve the electron density map. Twofold local medium NCS restraints were employed during refinement for residues 28–103, 110–158 and 194–260.

$K_{2P}2.1$, $K_{2P}2.1$–ML335 and $K_{2P}2.1$–ML402 structures have, respectively, 95.2%/0.4%, 92.0%/0.5% and 95.7%/0.4% residues in favoured regions/outliers of the Ramachandran plot as assessed by Molprobity[46].

Patch-clamp electrophysiology. Mouse $K_{2P}2.1$, human $K_{2P}4.1$, and mutants were expressed from a previously described pIRES2-EGFP vector[8,11] in HEK293T cells (ATTC). 70% confluent cells were transfected (in 35-mm diameter wells) with LipofectAMINE 2000 (Invitrogen) for 6 h, and plated onto coverslips coated with Matrigel (BD Biosciences).

Effects of ML335, ML402 and arachidonic acid on $K_{2P}2.1$ current at 0 mV were measured by whole-cell patch-clamp experiments 24 h after transfection. Acquisition and analysis were performed using pCLAMP9 and an Axopatch 200B amplifier (Molecular Devices). Pipette resistance ranged from 1 to 1.5 MΩ. Pipette solution contained the following: 145 mM KCl, 3 mM $MgCl_2$, 5 mM EGTA and 20 mM HEPES (pH 7.2 with KOH). Bath solution contained the following: 145 mM NaCl, 5 mM KCl, 1 mM $CaCl_2$, 3 mM $MgCl_2$ and 20 mM HEPES (pH 7.4 with NaOH). $K_{2P}2.1$ currents were elicited by a 1 s ramp from –100 to +50 mV from a –80 mV holding potential. After stabilization of the basal current, ML335 and ML402 were perfused at 200 ml per hour until potentiation was stably reached.

Voltage-dependent activation of $K_{2P}2.1$ was recorded on excised patches in inside-out configuration (50 kHz sampling) in the absence and presence of 5 μM ML335 or ML402. Pipette solution contained the following: 150 mM KCl, 3.6 mM $CaCl_2$, 10 mM HEPES (pH 7.4 with KOH). Bath solution contained the following: 150 mM RbCl, 2 mM EGTA and 10 mM HEPES (pH 7.4 with RbOH), and was continuously perfused at 200 ml per hour during the experiment. TREK-1 currents were elicited by a voltage step protocol from −100 mV to +100 mV, from a –80 mV holding potential (or −10 mV for $K_{2P}2.1$(G137I) and $K_{2P}4.1$(G124I) in presence of the compounds after exposing the patch to the compound for 30 s at −80 mV). Data were analysed using Clampfit 9 and Origin 7.

Two-electrode voltage-clamp electrophysiology. Two-electrode voltage-clamp recordings were performed on defolliculated stage V–VI *Xenopus laevis* oocytes 24–48 h after microinjection with 0.15–5 ng cRNA. Oocytes were impaled with borosilicate recording microelectrodes (0.3–3.0 MΩ resistance) backfilled with 3 M KCl. Recording solution (96 mM NaCl, 2 mM KCl, 1.8 mM $CaCl_2$, and 2.0 mM $MgCl_2$, buffered with 5 mM HEPES, pH 7.4) was perfused at a rate of 3 ml min^{-1}.

Currents were evoked from a −80 mV holding potential followed by a 300 ms ramp from −150 mV to +50 mV. Data were acquired using a GeneClamp 500B amplifier (MDS Analytical Technologies) controlled by pClamp software (Molecular Devices), and digitized at 1 kHz using Digidata 1332A digitizer (MDS Analytical Technologies).

Dose–response experiments were carried by first preparing a DMSO stock solution of each activator at a concentration of 100 mM. Owing to the low solubility of the compounds the highest tested concentrations in recording solution were 100 μM and 80 μM for ML335 and ML402, respectively (final concentration of DMSO

was 0.2%). Other concentrations were prepared by serial dilutions of the 100 μM solution in recording buffer supplemented with 0.1% DMSO.

Xenopus oocytes were collected in compliance with ethical regulations specified by the UCSF Institutional Animal Care and Use Committee protocol AN129690.

Synthetic chemistry. Detailed descriptions of synthesis routes and characterization of ML335, ML335a and ML402 are found in the supplementary material.

Data availability. Coordinates and structure factors have been deposited with the Protein Data Bank under accession codes 5VK5 (K_{2P}2.1), 5VKN (K_{2P}2.1–ML335) and 5VKP (K_{2P}2.1–ML402).

34. Kawate, T. & Gouaux, E. Fluorescence-detection size-exclusion chromatography for precrystallization screening of integral membrane proteins. *Structure* **14,** 673–681 (2006).
35. Drew, D. *et al.* GFP-based optimization scheme for the overexpression and purification of eukaryotic membrane proteins in *Saccharomyces cerevisiae*. *Nat. Protocols* **3,** 784–798 (2008).
36. Newstead, S., Kim, H., von Heijne, G., Iwata, S. & Drew, D. High-throughput fluorescent-based optimization of eukaryotic membrane protein overexpression and purification in *Saccharomyces cerevisiae*. *Proc. Natl Acad. Sci. USA* **104,** 13936–13941 (2007).
37. Kirchhofer, A. *et al.* Modulation of protein properties in living cells using nanobodies. *Nat. Struct. Mol. Biol.* **17,** 133–138 (2010).
38. Shaya, D. *et al.* Voltage-gated sodium channel (NaV) protein dissection creates a set of functional pore-only proteins. *Proc. Natl Acad. Sci. USA* **108,** 12313–12318 (2011).
39. Kabsch, W. Xds. *Acta Crystallogr. D* **66,** 125–132 (2010).
40. Evans, P. R. & Murshudov, G. N. How good are my data and what is the resolution? *Acta Crystallogr. D* **69,** 1204–1214 (2013).
41. Diederichs, K. & Karplus, P. A. Better models by discarding data? *Acta Crystallogr. D* **69,** 1215–1222 (2013).
42. Karplus, P. A. & Diederichs, K. Linking crystallographic model and data quality. *Science* **336,** 1030–1033 (2012).
43. Emsley, P. & Cowtan, K. Coot: model-building tools for molecular graphics. *Acta Crystallogr. D* **60,** 2126–2132 (2004).
44. Collaborative Computational Project, Number 4. The CCP4 suite: programs for protein crystallography. *Acta Crystallogr. D* **50,** 760–763 (1994).
45. Adams, P. D. *et al.* PHENIX: a comprehensive Python-based system for macromolecular structure solution. *Acta Crystallogr. D* **66,** 213–221 (2010).
46. Chen, V. B. *et al.* MolProbity: all-atom structure validation for macromolecular crystallography. *Acta Crystallogr. D* **66,** 12–21 (2010).
47. Zhou, Y., Morais-Cabral, J. H., Kaufman, A. & MacKinnon, R. Chemistry of ion coordination and hydration revealed by a K^+ channel-Fab complex at 2.0 Å resolution. *Nature* **414,** 43–48 (2001).
48. Guizouarn, H., Gabillat, N., Motais, R. & Borgese, F. Multiple transport functions of a red blood cell anion exchanger, tAE1: its role in cell volume regulation. *J. Physiol. (Lond.)* **535,** 497–506 (2001).
49. Rapp, C., Goldberger, E., Tishbi, N. & Kirshenbaum, R. Cation-π interactions of methylated ammonium ions: a quantum mechanical study. *Proteins* **82,** 1494–1502 (2014).
50. Crowley, P. B. & Golovin, A. Cation-pi interactions in protein-protein interfaces. *Proteins* **59,** 231–239 (2005).
51. Payandeh, J. & Minor, D. L., Jr. Bacterial voltage-gated sodium channels (BacNa(V)s) from the soil, sea, and salt lakes enlighten molecular mechanisms of electrical signaling and pharmacology in the brain and heart. *J. Mol. Biol.* **427,** 3–30 (2015).

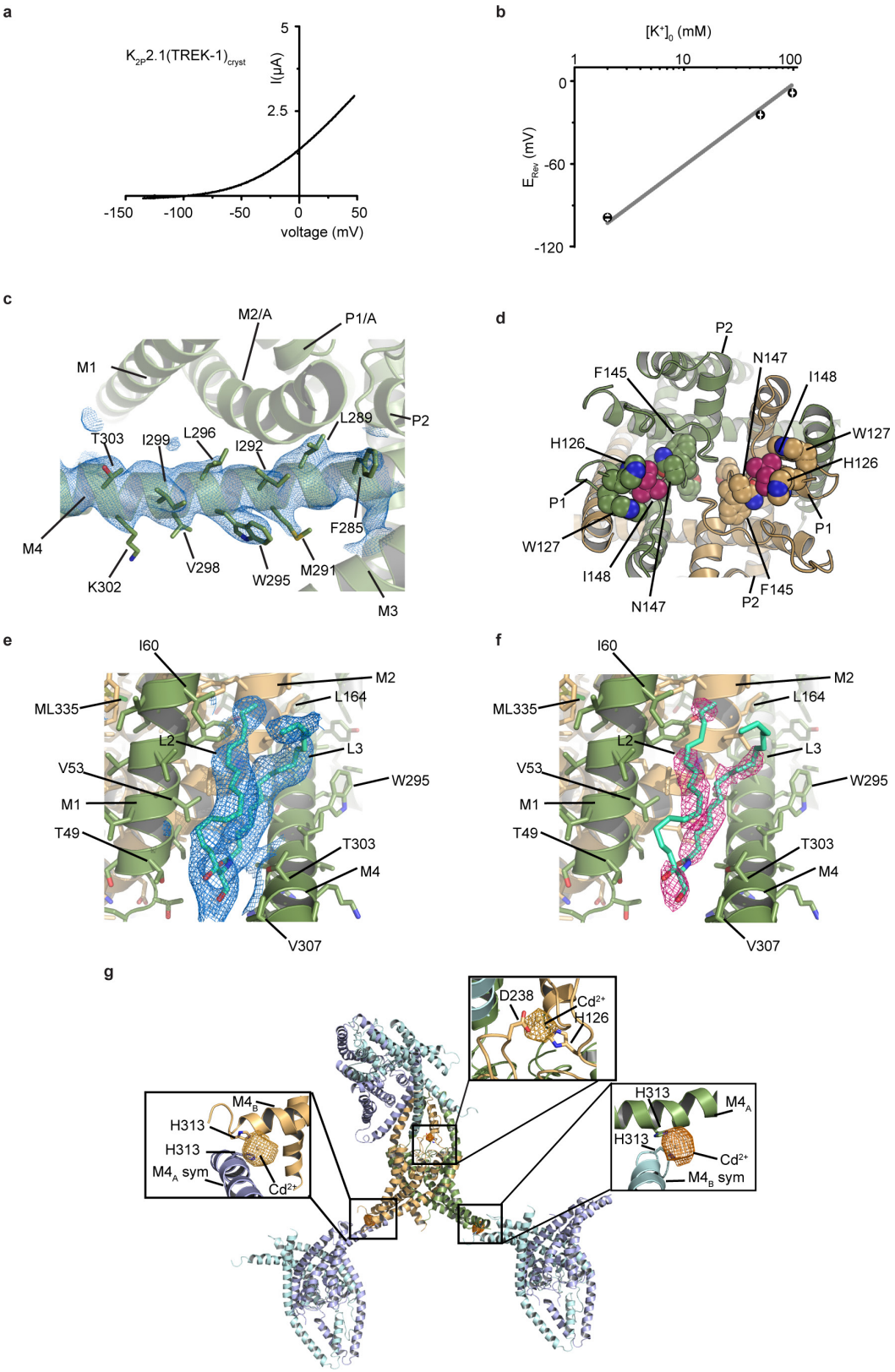

Extended Data Figure 1 | See next page for caption.

Extended Data Figure 1 | $K_{2P}2.1_{cryst}$ function and structure. a, Exemplar recording from $K_{2P}2.1_{cryst}$ expressed in *Xenopus* oocytes. Current was elicited from a −80 mV holding potential followed by a 500 ms ramp from −150 mV to +50 mV. **b**, $K_{2P}2.1_{cryst}$ potassium selectivity recorded in *Xenopus* oocytes in K^+/*N*-methyl-D-glucamine solutions (98.0 mM total) at $pH_o = 7.4$. Data represent mean ± s.e.m. ($n = 4$). Dashed grey line represents Nernst equation $E_{rev} = RT/F \times \log([K^+]_o/[K^+]_i)$, where R and F have their usual thermodynamic meanings, z is equal to 1, and $T = 23\,°C$, assuming $[K^+]_i = 108.6$ mM (ref. 48). **c**, Exemplar $2F_o - F_c$ electron density (1.0σ) for the C-tail region of $K_{2P}2.1_{cryst}$. Select residues and channel elements are indicated. **d**, Extracellular view of $K_{2P}2.1_{cryst}$ showing environment of His126 and Ile148 (purple). Select residues are labelled. The extracellular proton sensor $His126^{16,17}$ is supported by a highly conserved residue, Trp127, and contacts a gain-of-function mutant site, $Ile148^8$, that interacts with the selectivity filter residue Asn147. This network of physical interactions indicates how changes at $His126^{16,17}$ or $Ile148^8$ could affect the C-type gate. **e**, **f**, Exemplar L2/L3 lipid electron density for $K_{2P}2.1$–ML335. $2F_o - F_c$ (**e**; blue, 1.0σ) and $F_o - F_c$ (**f**; pink, 3.0σ). Chains are coloured smudge and light orange. Channel elements and select residues are labelled. **g**, Crystal lattice packing for $K_{2P}2.1_{cryst}$ showing that the C-tail makes lattice interactions stabilized by a cadmium ion coordinated between His313 of adjacent symmetry mates. Asymmetric unit is coloured smudge (chain A) and orange (chain B). Symmetry related channels are shown in slate (chain A) and cyan (chain B). Insets show the anomalous difference map (5.0σ) and locations of Cd^{2+} ions and their ligands. Colours defined according to PyMol, see https://pymolwiki.org/index.php/Color_Values for reference.

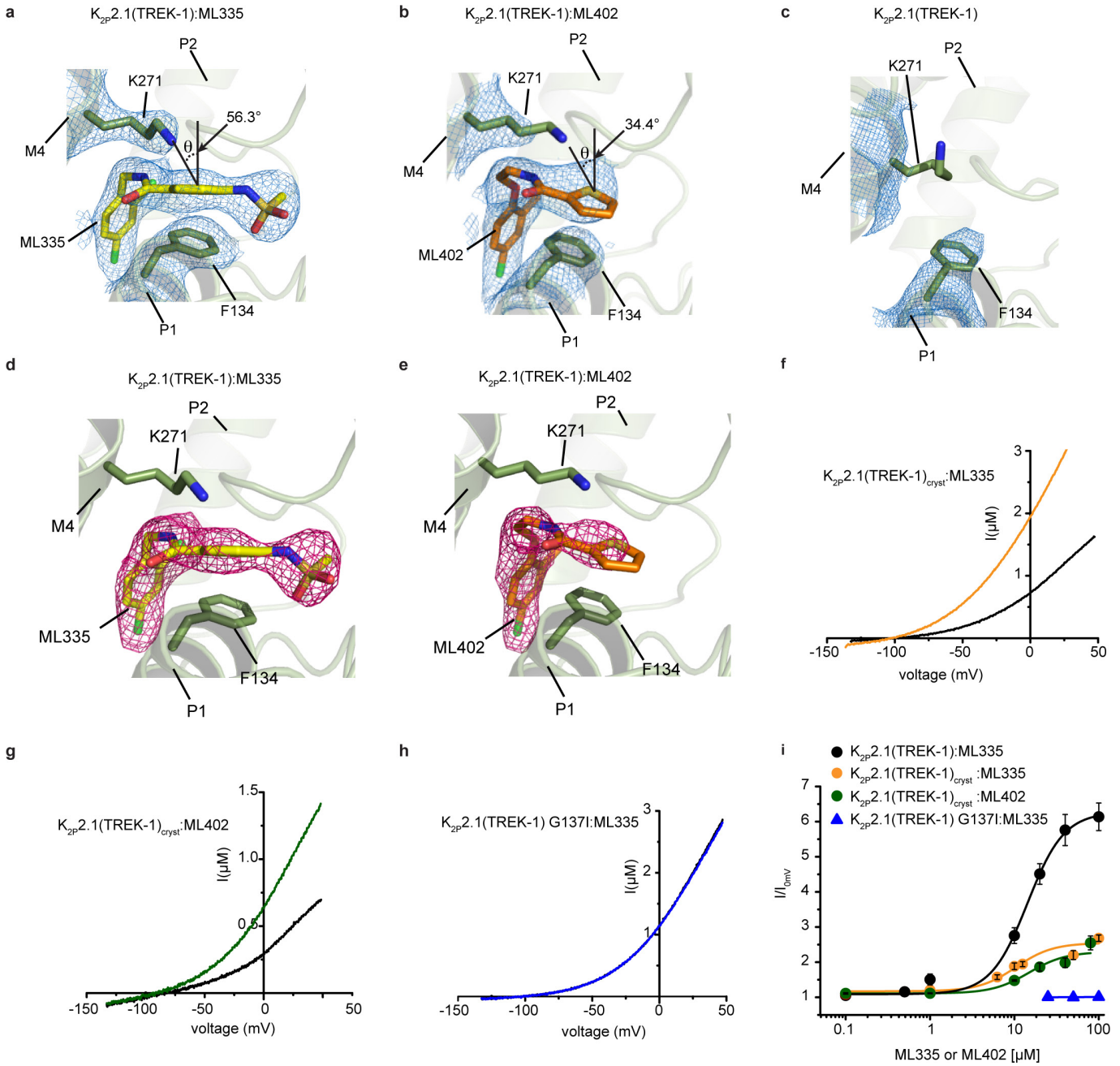

Extended Data Figure 2 | $K_{2P}2.1_{cryst}$ modulator binding pocket densities and $K_{2P}2.1_{cryst}$ functional properties. a–**e**, Exemplar electron densities for the modulator binding pockets. **a**–**c**, $2F_o - F_c$ densities (blue) for $K_{2P}2.1$–ML335 (**a**; 1.5σ), $K_{2P}2.1$–ML402 (**b**; 1.0σ) and K_{2P} 2.1 (**c**; 1.0σ). Offset angle for the cation–π interactions for Lys271–ML335 and Lys271–ML402 is shown and adopts an oblique geometry common to cation–π interactions[49,50]. **d**, **e**, $F_o - F_c$ densities (pink, 3.0σ) for $K_{2P}2.1$–ML335 (**d**) and $K_{2P}2.1$–ML402 (**e**). Final models are shown in all panels and select residues are shown and labelled. **f**–**h**, Exemplar current traces for $K_{2P}2.1_{cryst}$ (black) with 40 μM ML335 (orange) (**f**), $K_{2P}2.1_{cryst}$ (black) with 80 μM ML402 (green) (**g**) and $K_{2P}2.1$(G137I) (black) with 80 μM ML335 (blue) (**h**). **i**, Dose–response curves for $K_{2P}2.1$–ML335 (black), $EC_{50} = 14.3 \pm 2.7$ μM ($n \geq 5$); $K_{2P}2.1_{cryst}$–ML335, $EC_{50} = 10.5 \pm 2.7$ μM ($n \geq 3$) (yellow orange) $K_{2P}2.1_{cryst}$–ML402, $EC_{50} = 14.9 \pm 1.6$ μM ($n \geq 3$); and $K_{2P}2.1$(G137I)–ML335 (blue).

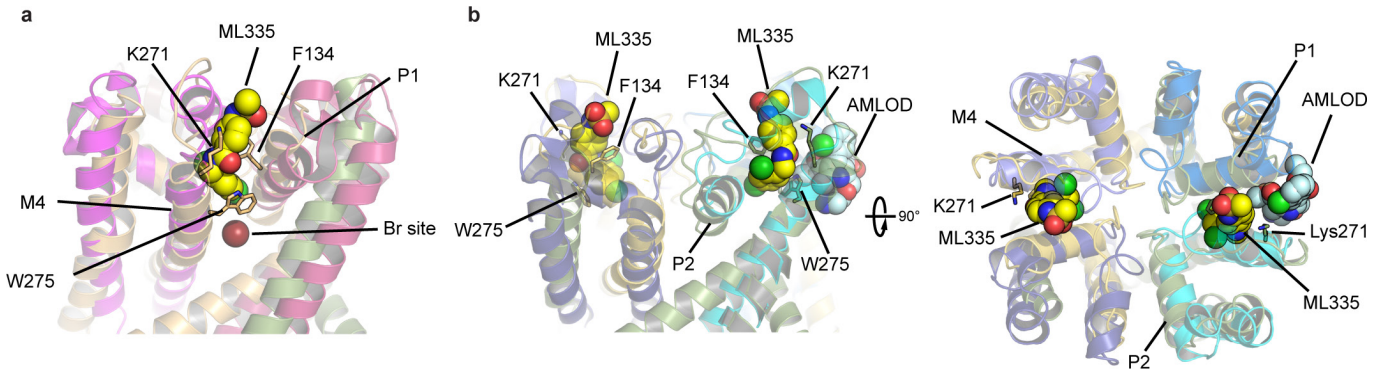

Extended Data Figure 3 | Comparison of K_{2P} modulator and VGIC antagonist sites. a, Superposition of the $K_{2P}2.1$–ML335 complex (smudge and orange) with the $BacNa_V$ 'pore-only' Na_VMs structure[18] (magenta and pink). Bromine site (Br) from labelled sodium channel antagonists is shown as a firebrick sphere. **b**, Superposition of the pore domains of the $K_{2P}2.1$–ML335 complex (smudge and orange) with the pore domain of the $BacNa_V$ Ca_VAb (5KMD) bound to the inhibitor amlodipine (AMLOD)[19], a site normally occupied by lipid[19,51]. Select residues of the K_{2P} modulator pocket are shown as sticks and are labelled. Ca_VAb subunits are coloured cyan, marine, slate and dark blue. ML335 (yellow) and amlodipine (cyan) are shown in space filling representation.

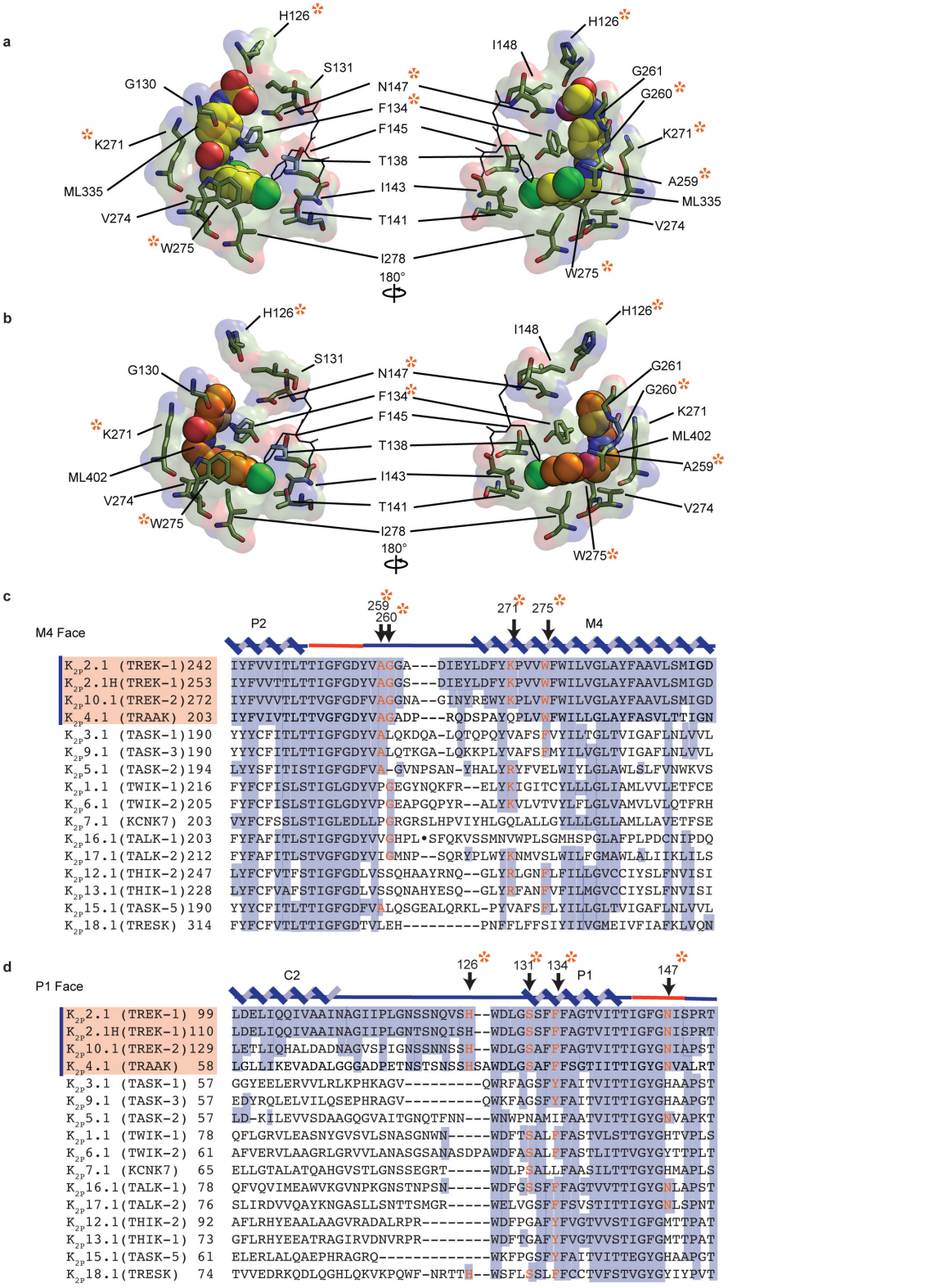

Extended Data Figure 4 | K_{2P} modulator pocket structure and conservation. **a**, **b**, Details of ML335 (**a**) and ML402 (**b**) interactions with $K_{2P}2.1$. **c**, **d**, Representative K_{2P} channel sequence comparisons for the M4 face (**c**) and P1 face (**d**). Purple bar and orange shading on sequence identifiers denotes the thermo- and mechanosensitive $K_{2P}2.1$ subfamily. Protein secondary structure is marked above the sequences. Selectivity filter region is in red. Residues involved in direct interactions with ML335 and ML402 are orange and marked with an orange asterisk. Conserved positions are highlighted. $K_{2P}2.1$ is the mouse protein used for this study. $K_{2P}2.1$H (TREK-1) is the human homologue. All other K_{2P} sequences are human origin. Sequences and identifiers are as follows: $K_{2P}2.1$, NP_034737.2; human $K_{2P}2.1$, NP_001017424.1; $K_{2P}10.1$, NP_612190.1; $K_{2P}4.1$, NP_001304019.1; $K_{2P}3.1$ (TASK-1), NP_002237.1; $K_{2P}9.1$ (TASK-3), NP_001269463.1; $K_{2P}5.1$ (TASK-2), NP_003731.1; $K_{2P}1.1$ (TWIK-1), NP_002236.103812.2; $K_{2P}6.1$ (TWIK-2), NP_004823.1; $K_{2P}7.1$ (KCNK7), AAI03812.2; $K_{2P}16.1$ (TALK-1), NP_001128577.1; $K_{2P}17.1$ (TALK-2), NP_113648.2; $K_{2P}12.1$ (THIK-2), NP_071338.1; $K_{2P}12.1$ (THIK-1), NP_071337.2; $K_{2P}15.1$ (TASK-5), NP_071753.2; and $K_{2P}18.1$ (TRESK), NP_862823.1. The dot in the $K_{2P}16.1$ (TALK-1) sequence in **c** denotes the following, non-conserved sequence that was removed to avoid a long alignment gap: NFITPSGLLPSQEPFQTPHGKPESQQIP.

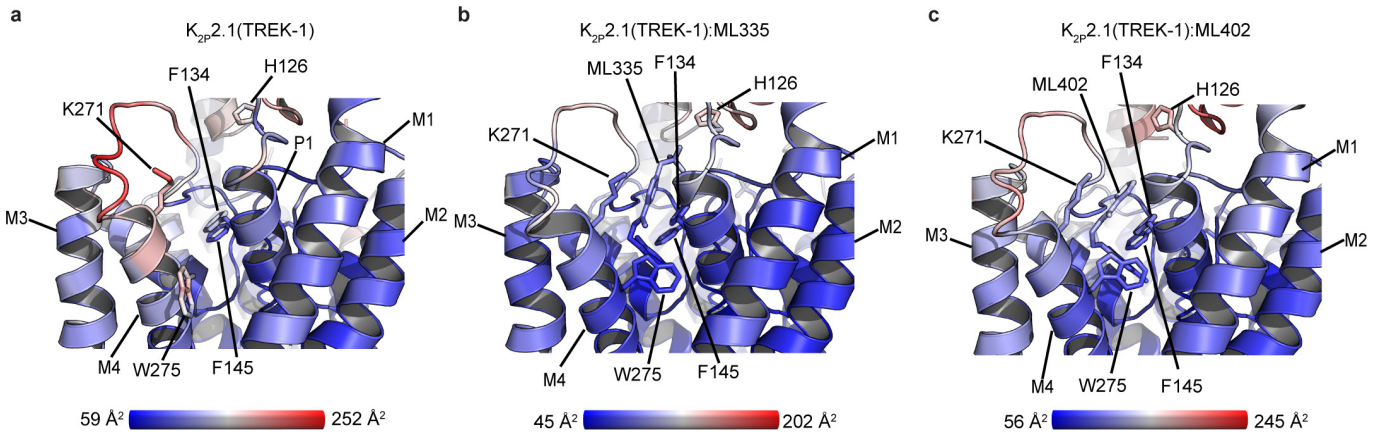

Extended Data Figure 5 | K_{2P} structure comparisons. K_{2P} modulator pocket views coloured by B-factor for K_{2P}2.1 (**a**), K_{2P}2.1–ML335 (**b**) and K_{2P}2.1–ML402 (**c**). Bars show B-factor scale.

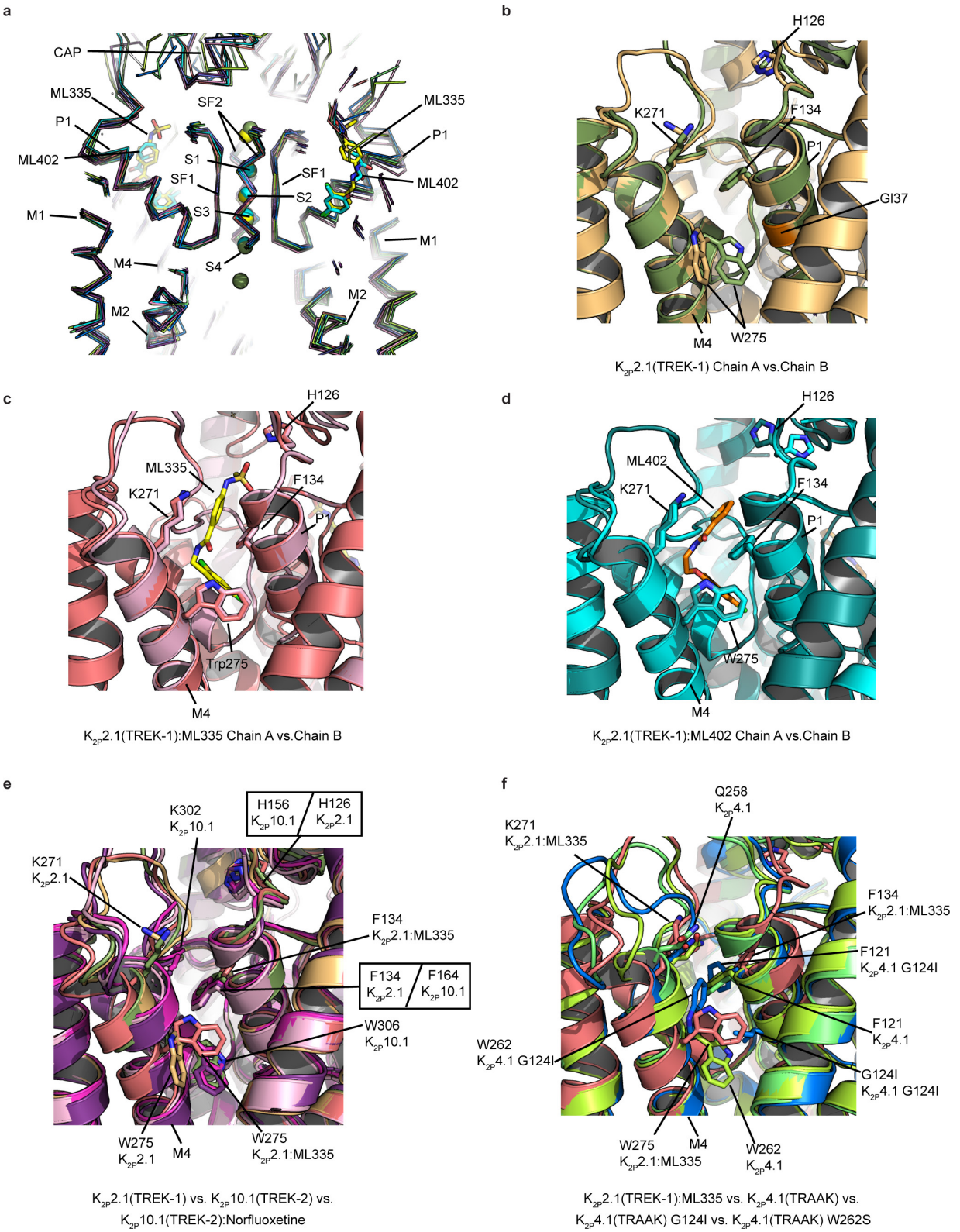

Extended Data Figure 6 | K_{2P} structure comparisons. a, Backbone atom superposition of $K_{2P}2.1$ (smudge, up), $K_{2P}2.1$–ML335 (yellow, up), $K_{2P}2.1$–ML402 (cyan, up), $K_{2P}10.1$ (4BW5) (pink, up)[6], $K_{2P}10.1$ (4XDJ) (magenta, down)[6], $K_{2P}10.1$–norfluoxetine (4XDK) (purple, down)[6], $K_{2P}4.1$ (4I9W) (limon, up)[13], $K_{2P}4.1$(G124I) (4RUE) (marine, down)[15], and $K_{2P}4.1$(W262S) (4RUF) (lime green, down)[15]. 'Up' or 'down' denotes M4 conformation. Selectivity filter ions for $K_{2P}2.1$ (smudge), $K_{2P}2.1$–ML335 (yellow), and $K_{2P}2.1$–ML402 (cyan) are shown as spheres. ML335 and ML402 are shown as sticks. Select channel elements are labelled. **b**, Superposition showing $K_{2P}2.1$ chain A (smudge) and chain B (light orange). Sites of gain-of-function mutations, G137I (orange)[7], and Trp275[8] are indicated. **c**, $K_{2P}2.1$–ML335 chain A (pink) and chain B (deep salmon), **d**, $K_{2P}2.1$–ML402 chain A (blue) and chain B (teal). **e**, $K_{2P}2.1$ chain A (smudge) and chain B (orange), $K_{2P}10.1$ (4BW5) (pink)[6], $K_{2P}10.1$ (4XDJ) (magenta)[6], $K_{2P}10.1$–norfluoxetine (4XDK) (purple)[6]. **f**, $K_{2P}2.1$–ML335 (pink), $K_{2P}4.1$ (4I9W) (limon)[13], $K_{2P}4.1$(G124I) (4RUE) (blue)[15], $K_{2P}4.1$(W262S) (4RUF) (lime green)[15]. G124I from $K_{2P}4.1$(G124I)[15] is shown as sticks. In **b**–**f**, Phe134, His126, Lys271, Trp275 and their equivalents in $K_{2P}10.1$, $K_{2P}4.1$ and $K_{2P}4.1$(G124I), are shown as sticks. In **c** and **d**, ML335 and ML402 are shown as sticks.

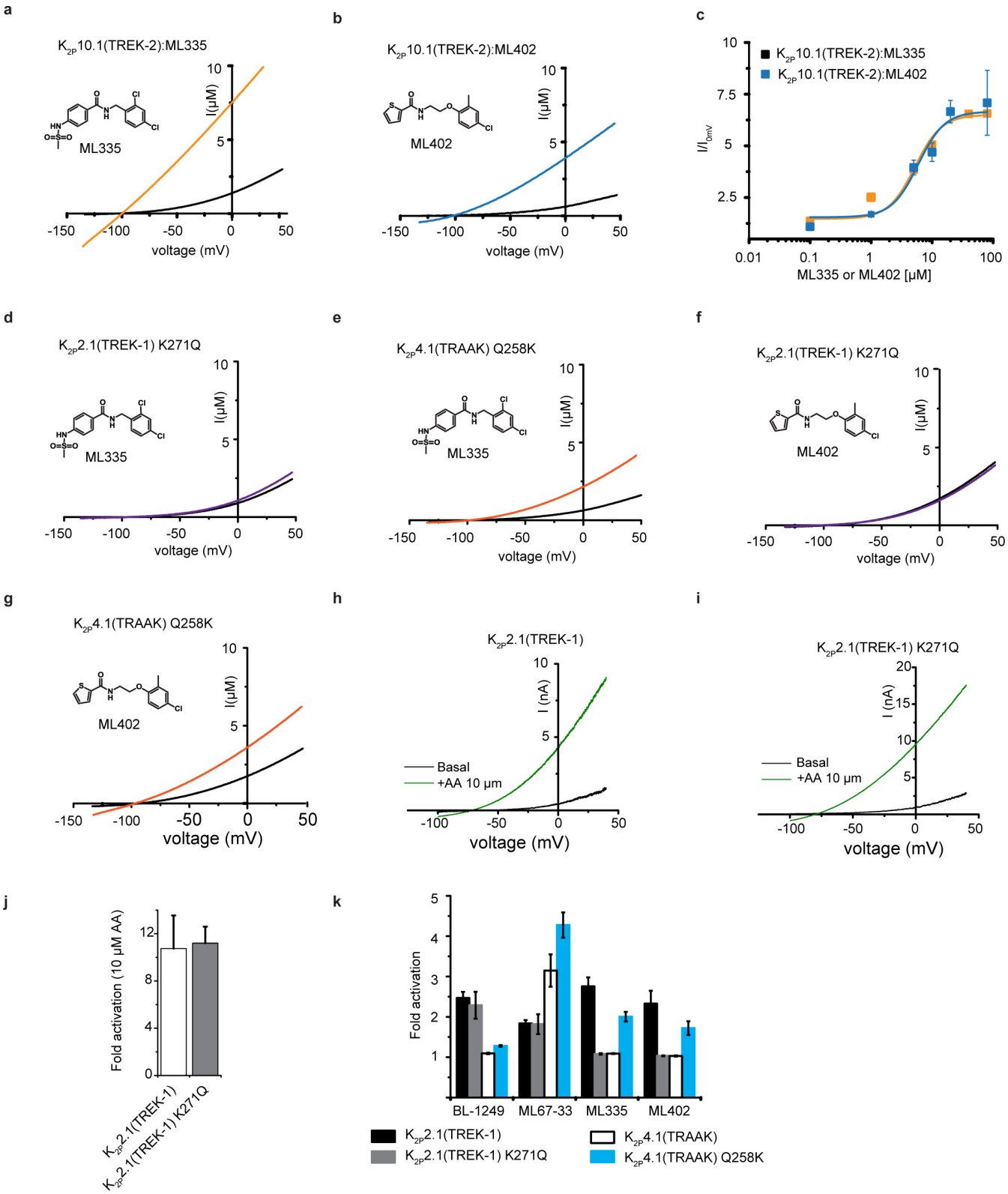

Extended Data Figure 7 | K_{2P} activator responses. a, **b**, Exemplar current traces for $K_{2P}10.1$ (black) with 20 μM ML335 (yellow orange) (**a**) and $K_{2P}10.1$ (black) with 20 μM ML402 (cyan) (**b**). **c**, Dose–response curves for $K_{2P}10.1$ with ML335 ($EC_{50} = 5.2 \pm 0.5$ μM ($n > 3$)) (yellow orange) and ML402 ($EC_{50} = 5.9 \pm 1.6$ μM ($n \geq 4$) (cyan). **d**–**g**, Exemplar current traces for $K_{2P}2.1$ K271Q (black) and with 20 μM ML335 (purple) (**d**); $K_{2P}4.1$(Q258K) (black) and with 50 μM ML335 (orange) (**e**); $K_{2P}2.1$(K271Q) (black) and with 50 μM ML402 (purple) (**f**); $K_{2P}4.1$(Q258K) (black) and with 50 μM ML402 (orange) (**g**). Currents were evoked from *Xenopus* oocytes expressing the indicated channels from a −80 mV holding potential followed by a 500 ms ramp from −150 mV to +50 mV. Compound structures are shown. **h**, **i**, Exemplar current traces for HEK293 cell inside-out patches expressing $K_{2P}2.1$ (**h**) and $K_{2P}2.1$(K271Q) (**i**) to stimulation by 10 μM arachidonic acid (AA) (green). **j**, Current potentiation measured in HEK cells at 0 mV in response to 10 μM arachidonic acid for $K_{2P}2.1$ ($n = 5$) and $K_{2P}2.1$(K271Q) ($n = 4$). **k**, Current potentiation measured in *Xenopus* oocytes at 0 mV for $K_{2P}4.1$ (white), $K_{2P}2.1$ (black), $K_{2P}4.1$(Q258K) (cyan) and $K_{2P}2.1$(K271Q) (grey) in response to 10 μM BL-1249, 30 μM ML67-33, and 20 μM ML335. For all experiments ($n \geq 4$). Data are mean ± s.e.m.

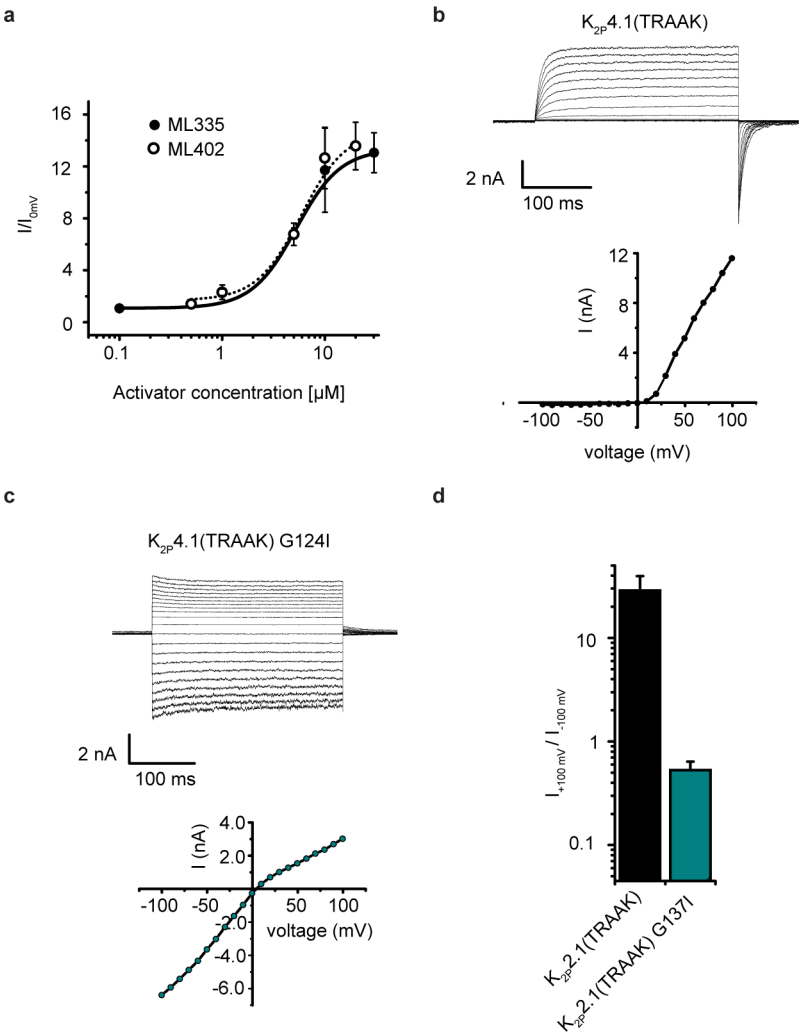

Extended Data Figure 8 | K_{2P} channel patch clamp recordings. a, Dose response for $K_{2P}2.1$ to ML335 (black circles) and ML402 (open circles) measured in HEK293 cells by whole-cell patch clamp. EC_{50} values are $5.2 \pm 0.8\,\mu M$ and $5.9 \pm 1.6\,\mu M$ for ML335 and ML402, respectively ($n \geq 3$). **b**, **c**, Representative current traces and voltage–current relationship from inside-out patches on HEK293 cells expressing $K_{2P}4.1$ (**b**) and $K_{2P}4.1$(G124I) (**c**) with a 350-ms voltage-step protocol from −100 mV to +100 mV in 150 mM $K^+_{[out]}$/150 mM $Rb^+_{[in]}$. **d**, Rectification coefficients ($I_{+100\,mV}/I_{-100\,mV}$) calculated from $n \geq 3$ current recordings obtained from the same conditions in **b** and **c**.

Extended Data Table 1 | Data collection and refinement statistics

	$K_{2P}2.1$(TREK-1) (5VK5)	$K_{2P}2.1$(TREK-1): ML335 (5VKN)	$K_{2P}2.1$ (TREK-1):ML402 (5VKP)
Data collection			
Space group	$P2_12_12_1$	$P2_12_12_1$	$P2_12_12_1$
Cell dimensions			
a, *b*, *c* (Å)	66.72/120.42 /126.44	67.07/119.39/128.18	67.09 / 119.56 / 127.21
α, β, γ (°)	90.0 / 90.0 / 90.0	90.0 / 90.0 / 90.0	90.0 / 90.0 / 90.0
Resolution (Å)	87.2 – 3.10 (3.21-3.10)	87.4 – 3.0 (3.11 – 3.0)	87.1 – 2.8 (2.99 – 2.8)
R_{merge} (%)	10.38 (>100%)	23.7 (>100%)	14.2 (>100%)
$I/\sigma(I)$	13.35 (0.3)	9.78 (0.66)	11.13 (0.37)
$CC_{1/2}$	0.999 (0.065)	0.998 (0.171)	0.999 (0.108)
Completeness (%)	97.0 (100.0)	97.0 (100.0)	98.0 (100.0)
Redundancy	6.0 (6.2)	12.9 (13.3)	12.8 (13.6)
Refinement			
Resolution (Å)	15.0 – 3.10 (3.21-3.10)	15.0 – 3.0 (3.11 – 3.0)	15.0 – 2.8 (2.99 – 2.8)
No. reflections	18506	20686	25882
R_{work} / R_{free}	26.1 / 31.4	25.8 / 28.3	26.9 / 31.4
No. atoms			
Protein	4289	4357	4328
Ligand/ion	74	200	174
K^+	6	6	6
Cd^{2+}	3	3	1
Lipid	65	191	167
ML335 or ML402			
Water	0	0	0
B factors			
Protein	154.6	107.4	147.7
Ligand/ion	168.7	96.5	131.0
Water	n/a	n/a	n/a
R.m.s. deviations			
Bond lengths (Å)	0.002	0.006	0.002
Bond angles (°)	0.480	0.685	0.483

Values in parentheses are for highest-resolution shell. Each dataset was derived from a single crystal.

Extended Data Table 2 | $K_{2P}2.1$ B-factor and structure comparisons

		B-factor (Å^2)		
Location	Residue	$K_{2P}2.1$ (TREK-1)	$K_{2P}2.1$ (TREK-1):ML335	$K_{2P}2.1$ (TREK-1):ML402
Selectivity filter	Gly144	108.6	63.0	92.7
	Phe145	109.7	64.7	98.4
	Gly146	118.5	76.5	127.4
Modulator pocket	Phe134	139.3	74.0	104.1
	Lys271	181.9	83.0	116.1
	Trp275	156.5	69.9	103.2
Channel core		132.4	83.5	118.8

Extended Data Table 2b | Structural comparisons with $K_{2P}2.1$(TREK-1)

PDB code	K_{2P}	Cα RMSD (Å) (ΔCAP, ΔM4)	Cα RMSD(Å) Channel core (ΔCAP, ΔM2, ΔM4)
5VKN	$K_{2P}2.1$(TREK-1):ML335	0.443	0.388
5VKP	$K_{2P}2.1$(TREK-1):ML402	0.462	0.426
4XDK	$K_{2P}10.1$(TREK-2):Norfluoxetine	1.976	1.317
4BW5	$K_{2P}10.1$(TREK-2):M4 up	1.054	0.918
4XDJ	$K_{2P}10.1$(TREK-2):M4 down	1.790	1.331
4I9W	$K_{2P}4.1$(TRAAK)	1.176	1.141
3UM7	$K_{2P}4.1$(TRAAK) (no domain swap)	1.468	1.390
4RUF	$K_{2P}4.1$(TRAAK) W262S	1.351	1.288
4RUE	$K_{2P}4.1$(TRAAK) G124I	1.466	1.490
4WFF	$K_{2P}4.1$(TRAAK) M4 down	1.155	1.217
4WFE	$K_{2P}4.1$(TRAAK) M4 up	1.149	1.023

a, B-factor comparisons. Selectivity-filter-residue B-factors are below the average channel-core B-factor in both the $K_{2P}2.1$ and modulator-bound structures. Modulator-pocket-residue B-factors drop relative to the average B-factor in both the ML335 and ML402 complexes, indicating that modulator binding reduces the mobility of these residues. The structures are determined in ~200 mM potassium, a concentration that is expected to stabilize the conformation of the selectivity filter (compare with ref. 47) and that could mask mobility changes. Average B-factor is calculated using the channel core elements on both chains: M1 (residues 47–65), P1 through common part of M2 (residues 127–188), common part of M3 through common part M4 (residues 210–300). The selectivity filter was included in the calculation. Blue and red values are >10% below or above the average B-factor, respectively. **b,** K_{2P} channel structure comparisons. Root mean square deviations (RMSDs) are calculated using the following $K_{2P}2.1$ (5VK5) chain A and chain B elements: (ΔCAP, ΔM4), M1 through cap (residues 47–69), P1 through common part of M4 (residues 127–281); channel core (ΔCAP, ΔM2, ΔM4), M1 (residues 47–65), P1 through common part of M2 (residues 127–188), common part of M3 through common part M4 (residues 210–300). The selectivity filter was included in the calculation. For the non-domain-swapped $K_{2P}4.1$ (3UM7), residues 47–69 of chain A were compared to equivalent chain B residues.

doi:10.1038/nature22988

Synthetic chemistry

ML335 and ML402 were identified as $K_{2P}2.1$(TREK-1) activators using a combination of fluorescence-based thallium flux and automated patch-clamp assays. ML335, ML402, and ML335a were synthesized using chemical synthesis procedures outlined below. ML335 was also purchased from Chembridge.

Scheme 1: Synthesis of ML335

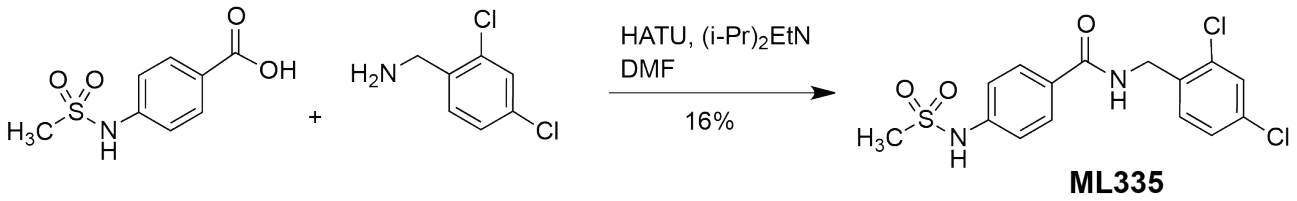

Step 1: Preparation of N-[(2,4-dichlorophenyl)methyl]-4-methanesulfonamidobenzamide (ML335)

A 50 ml reaction bottle equipped with a magnetic stirbar was charged with 2,4-dichlorobenzylamine (100 µl, 0.7 mmol, 1.0 equiv.), 4-(methanesulfonylamino)benzoic acid (0.160 g, 0.7 mmol, 1.0 equiv.) and N,N-dimethylformamide (2.000 ml). To the mixture was added HATU (0.424 g, 1.1 mmol, 1.5 equiv.) followed by triethylamine (0.311 ml, 2.2 mmol, 3.0 equiv.) The reaction mixture was stirred for 3 hours at room temperature and then partitioned between ethyl acetate and 10% aqueous citric acid. The organic layer was separated and washed with brine, then dried over Na_2SO_4, decanted, and concentrated. The crude residue was re-suspended in dichloromethane and purified by automated silica gel flash chromatography on a 12g silica gel cartridge, using gradient elution with 0-100% of ethyl acetate in hexane. Pure fractions were collected and concentrated to afford 44 mg of the desired product N-[(2,4-dichlorophenyl)methyl]-4-methanesulfonamidobenzamide (16.0 % yield).

^{1}H NMR (300 MHz, DMSO-d6) δ ppm 3.07 (s, 3 H) 4.49 (d, J=5.46 Hz, 2 H) 7.26 (m, J=8.67 Hz, 2 H) 7.34 (d, J=8.67 Hz, 1 H) 7.41 (d, J=8.10 Hz, 1 H) 7.62 (s, 1 H) 7.89 (m, J=8.48 Hz, 2 H) 8.99 (br. s., 1 H) 10.15 (s, 1 H)

^{13}C NMR (75 MHz, DMSO-*d*6) δ ppm 39.68, 40.24, 118.01, 127.32, 128.57, 128.66, 128.81, 130.01, 132.17, 132.88, 135.73, 141.46,165.89

LCMS predicted: m/z: m/z: 372.01 (100.0%), 374.01 (69.3%), 373.01 (17.9%), 376.00 (13.1%), 375.01 (11.8%), 377.01 (2.3%), 376.01 (1.5%), 374.02 (1.3%) seen: $[M+H]^+$ (major) 373.0, 374.9 also $[M+CH_3CN+H]^+$ (major) 413.9, 415.9

Scheme 2: Synthesis of ML402

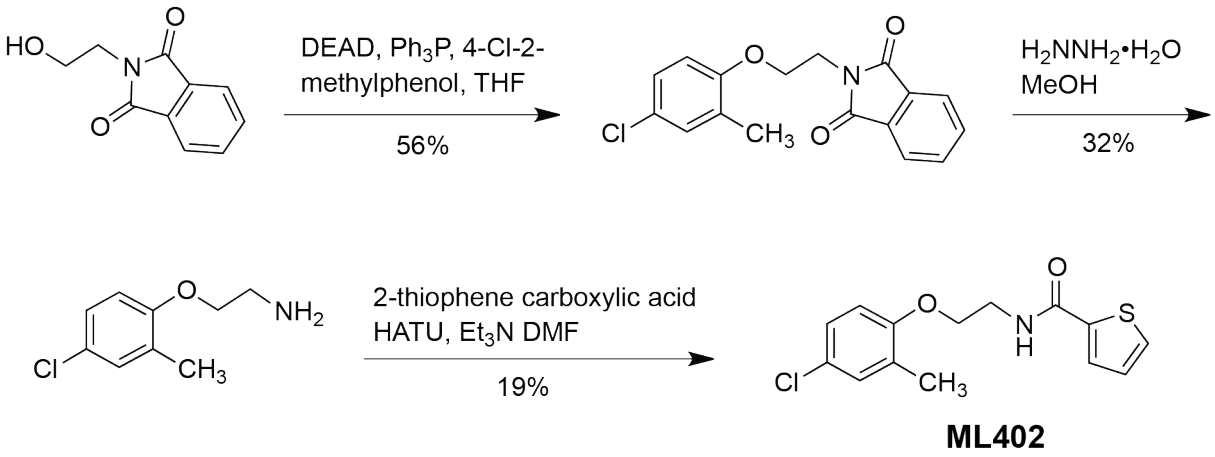

ML402

Step 1: Preparation of 2-[2-(4-chloro-2-methylphenoxy)ethyl]-2,3-dihydro-1H-isoindole-1,3-dione

The preparation of this known compound was based on that described [1]. A solution of diethyl azodicarboxylate (3.583 ml, 7.8 mmol, 1.5 equiv.) in dry THF (25 ml) was added under dry nitrogen to a solution of 2-(4-chlorophenoxy) ethylamine (1.0 g, 5.2 mmol, 1.0 equiv.), triphenylphosphine (2.06 g, 7.8 mmol, 1.5 equiv.) and 4-chloro-2-methylphenol (1.19 g, 7.8 mmol, 1.5 equiv.) in dry THF (50 ml). The reaction mixture was stirred at room temperature overnight then concentrated. The residue was re-suspended in diethyl ether and the solid filtered off on Celite. The filtrate was concentrated and the residue was re-dissolved in dichloromethane and then purified by silica gel chromatography on an 80 g silica gel cartridge using gradient elution with 0-20% ethyl acetate in hexane to afford 0.92 g of the desired product 2- [2- (4-chloro-2-methylphenoxy)ethyl] -2,3-dihydro-1H-isoindole-1,3-dione (56 % yield).

Step 2: Preparation of 1-(2-aminoethoxy)-4-chloro-2-methylbenzene

Deprotection of the amine function was accomplished according to the procedure described in [2]. A 50 ml reaction bottle with a magnetic stir bar was charged with 2-[2-(4-chloro-2-methylphenoxy)ethyl]-2,3-dihydro-1H-isoindole-1,3-dione (417 mg, 1.3 mmol, 1.0 equiv.) and methanol (20 ml) was added, followed by hydrazine monohydrate (500 µL, 10.3 mmol, 7.8 equiv.). The reaction mixture was stirred for 72 hours at room temperature after which time the reaction was judged complete. The solvent was evaporated chloroform was added, the organic layer was washed with water and brine and then dried over Na_2SO_4, decanted, and concentrated. The residue was re-suspended in dichloromethane and applied purified by silica gel chromatography on a 12g silica gel cartridge using gradient elution 1-10% of 1% NH_4OH in methanol in dichloromethane to afford 79 mg of the desired product 1-(2-aminoethoxy)-4-chloro-2-methylbenzene (32 % yield).

^{1}H NMR (300 MHz, CHLOROFORM-d) δ ppm 2.19 (s, 3 H) 3.09 (t,J=4.90 Hz, 2 H) 3.43 (s, 2 H) 3.95 (t, J=5.09 Hz, 2 H) 6.71 (d, J=8.29 Hz, 1H) 7.01 - 7.15 (m, 2 H)

^{13}C NMR (75 MHz, CHLOROFORM-d) δ ppm 16.45, 41.81, 70.59, 112.39, 125.50, 126.70, 128.94, 130.76, 155.82

LCMS (done on crude reaction mixture), predicted: m/z: 185.06 (100.0%), 187.06 (32.2%), 186.06 (10.1%), 188.06 (3.2%) seen: $[M+H]^+$ (major) = 186.1, also $[M+CH_3CN+H]^+$ 227.1, 229.1

Step 3: Preparation of N-[2-(4-chloro-2-methylphenoxy)ethyl]thiophene-2-carboxamide (ML402)

A 50 ml reaction bottle with a magnetic stirbar was charged with 1-(2-aminoethoxy)-4-chloro-2-methylbenzene (39 mg, 0.2 mmol, 1.0 equiv.), thiophene-2-carboxylic acid (27 mg, 0.2 mmol, 1.0 equiv.) and N,N-dimethylformamide (2.000 mL, 25.9 mmol, 122.4 equiv.). To the mixture was added added HATU (121 mg, 0.3 mmol, 1.5 equiv.) followed by triethylamine (89 µL, 0.6 mmol, 3.0 equiv.) The reaction mixture was stirred for 3 hours at room temperature and then partitioned between ethyl acetate and 10% aqueous citric acid. The organic layer was separated and washed with brine, then dried over Na_2SO_4, decanted, and concentrated. The residue was re-suspended in dichloromethane and purified by automated silica gel flash chromatography on a 12g silica gel cartridge, using gradient elution with 0-100% of ethyl acetate in hexane. The resulting residue (18.5mg) was further purified by preparative HPLC (C18 column, 40% to 90% methanol in water, 0.05% formic acid) to afford 12 mg of the desired product N-[2-(4-chloro-2-methylphenoxy)ethyl]thiophene-2-carboxamide (19 % yield).

^{1}H NMR (300 MHz, CHLOROFORM-d) δ ppm 2.24 (s, 3 H) 3.89 (q, J=5.27 Hz, 2 H) 4.14 (t, J=5.50 Hz, 2 H) 6.48 (br. s., 1 H) 6.76 (d, J=8.10 Hz, 1 H) 7.06 - 7.17 (m, 3 H) 7.51 (d, J=5.09 Hz, 1 H) 7.54 (d, J=3.58 Hz, 1 H)

^{13}C NMR (75 MHz, CHLOROFORM-*d*) δ ppm 16.18, 39.39, 67.08, 112.30, 125.66, 126.52, 127.69, 128.25, 128.49, 130.06, 130.54, 138.45, 155.08, 161.95

LCMS predicted: m/z: 295.04 (100.0%), 297.04 (36.5%), 296.05 (15.4%), 298.04 (5.9%), 299.04 (1.7%), 297.05 (1.6%), 296.04 (1.2%) seen: $[M+H]^+$ (major) 296.1, 298.1

Scheme 3: Synthesis of ML335a

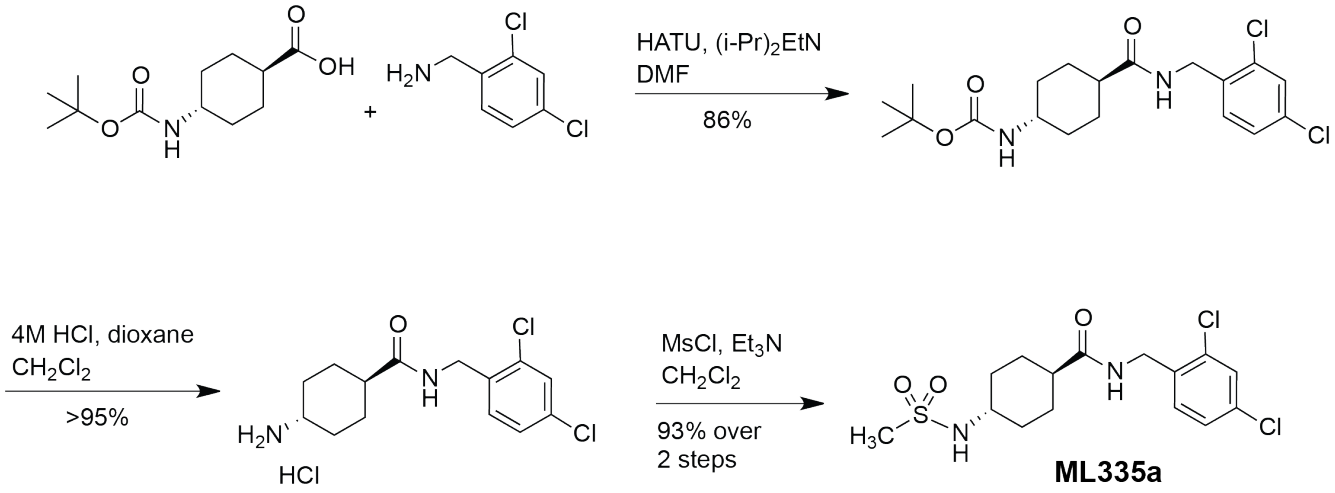

Step 1: Preparation of trans tert-butyl N-(4-{[(2,4-dichlorophenyl)methyl]carbamoyl}cyclohexyl)carbamate

A round bottom flask was charged with Boc-trans-1,4-aminocyclohexane carboxylic acid (181 mg, 0.7 mmol, 1.0 equiv.) and N,N-dimethylformamide (5 mL). To the mixture was added added HATU (424 mg, 1.1 mmol, 1.5 equiv.) followed by 2,4-dichlorobenzylamine (100 µL, 0.7 mmol, 1.0 equiv.), and finally triethylamine (0.31 mL, 2.2 mmol, 3.0 equiv.). The reaction mixture was stirred for an hour at room temperature and then diluted with ethyl acetate and 10% aqueous citric acid. The organic layer was separated and washed with brine, leading to the formation of a precipitate. The entire two-phase mixture was therefore filtered and the precipitate collected on a paper filter. This afforded the product, trans tert-butyl N-(4-{[(2,4-dichlorophenyl)methyl]carbamoyl}cyclohexyl)carbamate (257 mg, 0.6 mmol, 86%), which was used in the next step without further purification.

^{1}H NMR (300 MHz, CHLOROFORM-d) δ ppm 1.10 (dd, J=11.87, 3.39 Hz, 2 H) 1.44 (s, 8 H) 1.57 (dd, J=12.34, 3.30 Hz, 2 H) 1.93 (d, J=13.38 Hz, 2 H) 1.98 - 2.18 (m, 3 H) 4.47 (d, J=6.03 Hz, 2 H) 5.93 (br. s., 1 H) 7.21 (dd, J=8.19, 1.98 Hz, 1 H) 7.31 (d, J=8.29 Hz, 1 H) 7.38 (d, J=2.07 Hz, 1 H) LCMS: predicted: m/z: 400.13 (100.0%), 402.13 (64.1%), 401.14 (21.0%), 403.13 (13.7%), 404.13 (10.7%), 402.14 (2.7%), 405.13 (2.2%), 404.14 (1.3%) Seen: (only fragment, m-15 observed (major): 386.1, 388.1

Step 2: Preparation of trans-4-amino-N-[(2,4-dichlorophenyl)methyl]cyclohexane-1-carboxamide hydrochloride

A 25 mL round-bottom flask was charged with trans tert-butyl N-(4-{[(2,4-dichlorophenyl)methyl]carbamoyl}cyclohexyl)carbamate (257 mg, 0.6 mmol) dissolved in dichloromethane (4.0 ml) with stirring, and then treated with a hydrochloric acid solution (4.0 ml of 4M

solution in 1,4 dioxane, 16.0 mmol, 25.0 equiv.). The reaction mixture was stirred overnight and then the solvent was evaporated to afford crude trans-4-amino-N-[(2,4-dichlorophenyl)methyl]cyclohexane-1-carboxamide hydrochloride (244 mg, 0.7 mmol), which was used in the next step without further purification.

^{1}H NMR (300 MHz, DMSO-d6) δ ppm 1.26 - 1.57 (m, 4 H) 1.83 (d, J=12.06 Hz, 2 H) 2.00 (d, J=9.61 Hz, 2 H) 2.19 (m., 1 H) 2.95 (br. s., 1 H) 4.27 (d, J=5.27 Hz, 1 H) 7.30 (d, J=8.29 Hz, 1 H) 7.42 (d, J=8.85 Hz, 1 H) 7.61 (s, 1 H) 8.15 (br. s., 2 H) 8.46 (t, J=5.5 Hz, 1 H)

LCMS, predicted: m/z: 300.08 (100.0%), 302.08 (64.2%), 301.08 (15.9%), 304.07 (10.2%), 303.08 (9.8%), 305.08 (1.6%), 302.09 (1.1%) seen: $[M+H]^{+}$ (major) = 300.89, 302.91

Step 3: Preparation of trans-N-[(2,4-dichlorophenyl)methyl]-4-ethenesulfonamidocyclohexane-1-carboxamide

A 25 mL round bottom flask was charged with trans-4-amino-N-[(2,4-dichlorophenyl)methyl]cyclohexane-1-carboxamide hydrochloride (50 mg, 0.1 mmol, 1.3 equiv.) dissolved in dichloromethane (2.5 ml). The mixture was stirred in an ice bath and treated with triethylamine (0.083 ml, 0.6 mmol, 5.3 equiv.), followed by methanesulfonyl chloride (9 µl, 0.1 mmol, 1.0 equiv.). The reaction mixture was stirred for 3 hours while warming to room temperature. During the reaction a precipitate formed, and this was collected by vacuum filtration on a paper filter. The solid was saved and the filtrate was applied directly on a 12g silica gel cartridge and purified using gradient elution (0-100% ethyl acetate in hexanes). Relevant fractions were collected and concentrated to afford 19.5 mg of the product, which was identical to the precipitate collected directly from the reaction mixture. Combined, this amounted to 39 mg of the desired product, trans-N-[(2,4-dichlorophenyl)methyl]-4-ethenesulfonamidocyclohexane-1-carboxamide (0.1 mmol, 93% over two steps).

^{1}H NMR (300 MHz, DMSO-d6) δ ppm 1.20 (m, 2 H) 1.43 (m 2 H) 1.76 (d, J=10.36 Hz, 2 H) 1.92 (d, J=9.23 Hz, 2 H) 2.03-2.20 (m, 1 H) 2.89 (s, 3 H) 2.98 - 3.16 (m, 1 H) 4.25 (d, J=5.84 Hz, 2 H) 6.98 (d, J=7.54 Hz, 1 H) 7.26 (d, J=8.10 Hz, 1 H) 7.41 (dd, J=8.38, 2.17Hz, 1 H) 7.59 (d, J=2.07 Hz, 1 H) 8.29 (t, J=5.50 Hz, 1 H)

^{13}C NMR (100 MHz, DMSO-d6) δ ppm 28.19, 32.92, 39.38, 41.00, 42.70, 51.49, 127.30, 128.53, 129.91, 132.08, 132.89, 135.77, 174.92

LCMS: Predicted: m/z: 378.06 (100.0%), 380.05 (68.4%), 379.06 (17.4%), 382.05 (13.2%), 381.06 (11.5%), 383.05 (2.3%), 380.06 (2.1%), 382.06 (1.4%), 381.05 (1.0%), observed (m/z): $[M+H]^{+}$ = (major) 379.1, 381.1

References

1. Pascale, R. *et al.* New N-(phenoxydecyl)phthalimide derivatives displaying potent inhibition activity towards alpha-glucosidase. *Bioorg Med Chem* **18**, 5903-5914, doi:10.1016/j.bmc.2010.06.088 (2010).
2. Eguchi, Y., Sasaki, F., Sugimoto, A., Ebisawa, H. & Ishikawa, M. Studies on Hypotensive Agents - Synthesis of 1-Substituted 3-(2-Chlorophenyl)-6-Ethoxycarbonyl-5,7-Dimethyl-2,4(1h,3h)-Quinazolinediones. *Chem Pharm Bull* **39**, 1753-1759 (1991).

ML335-^{1}H

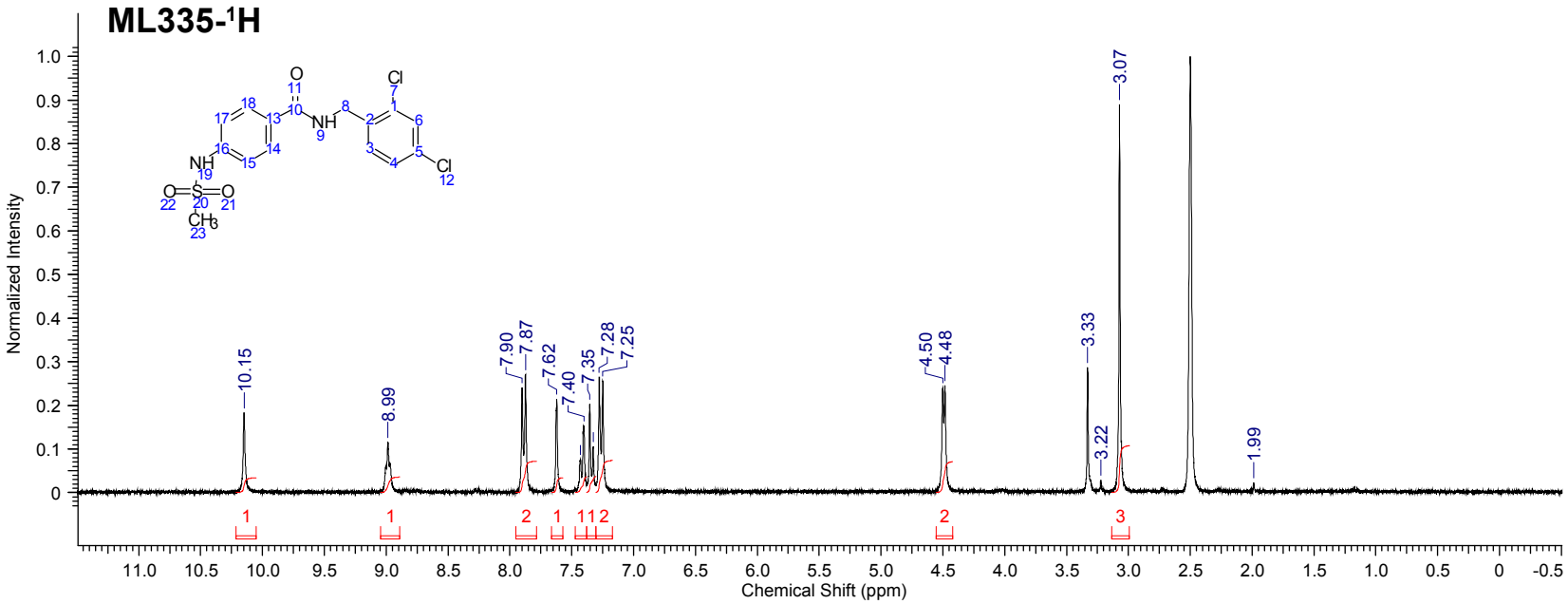

ML335-^{13}C

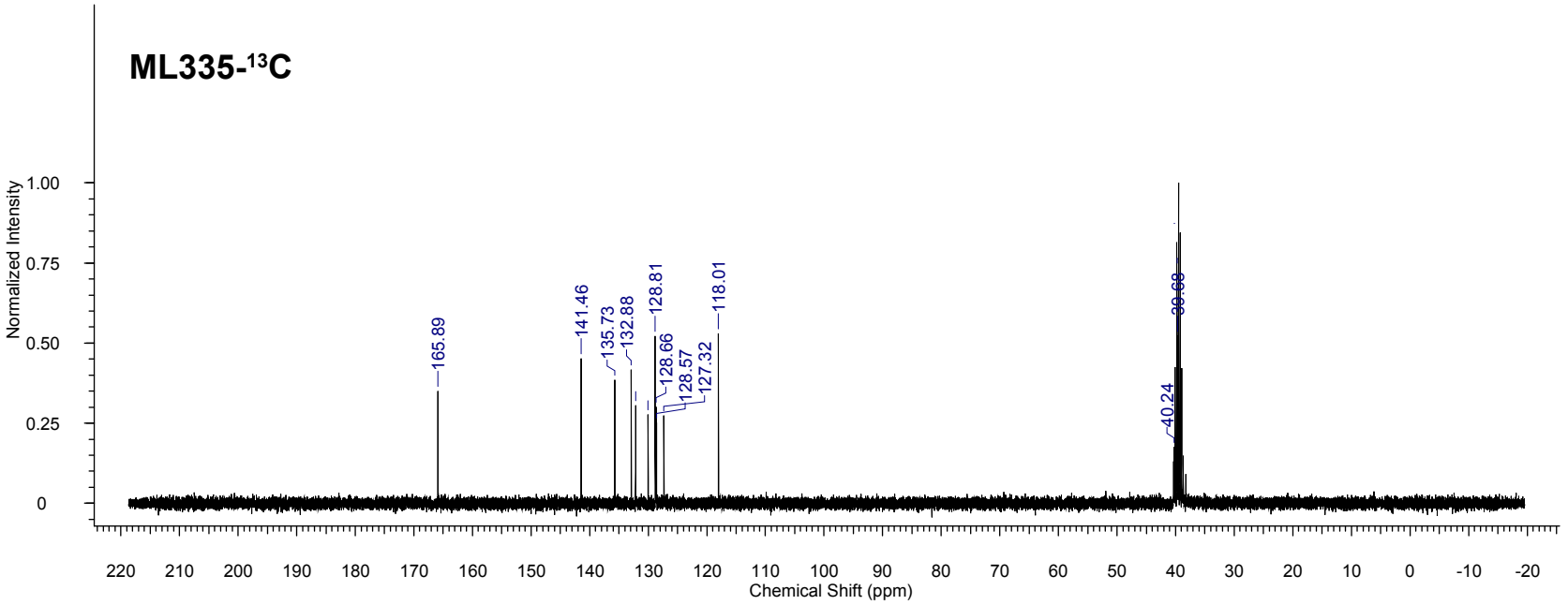

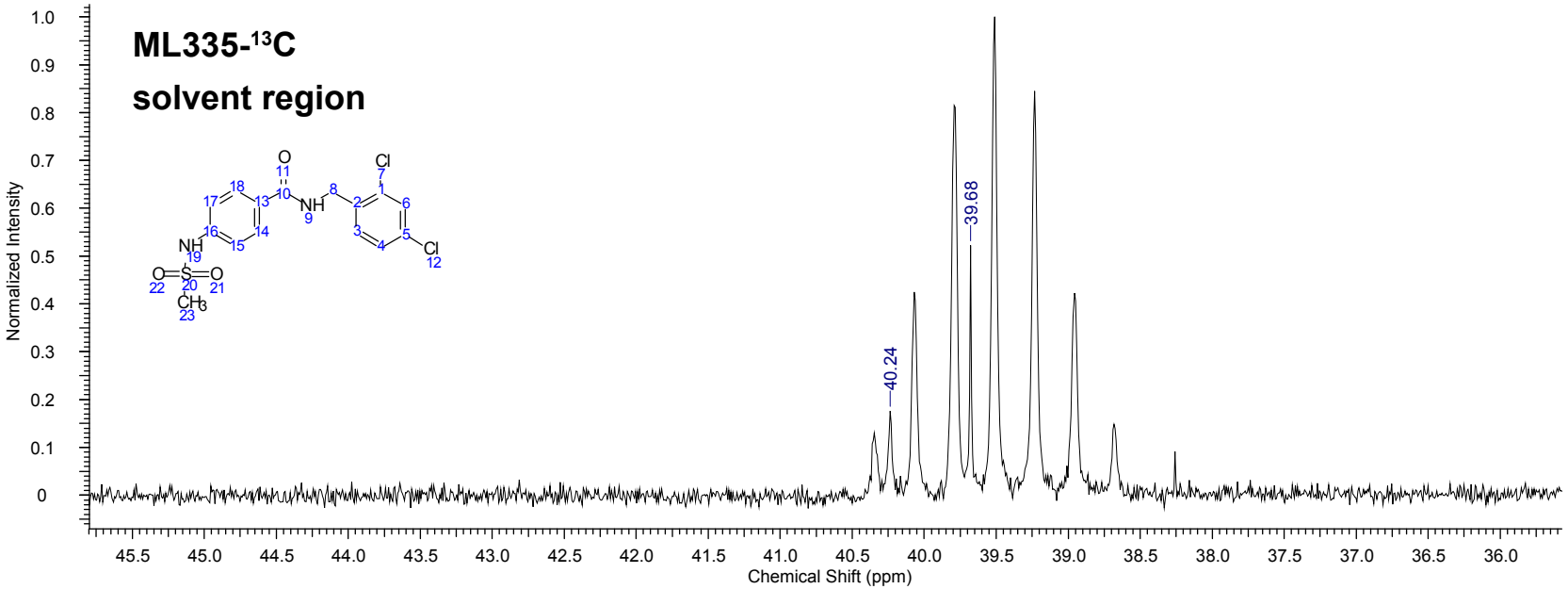
ML335-13C
solvent region
Normalized Intensity
Chemical Shift (ppm)
40.24
39.68

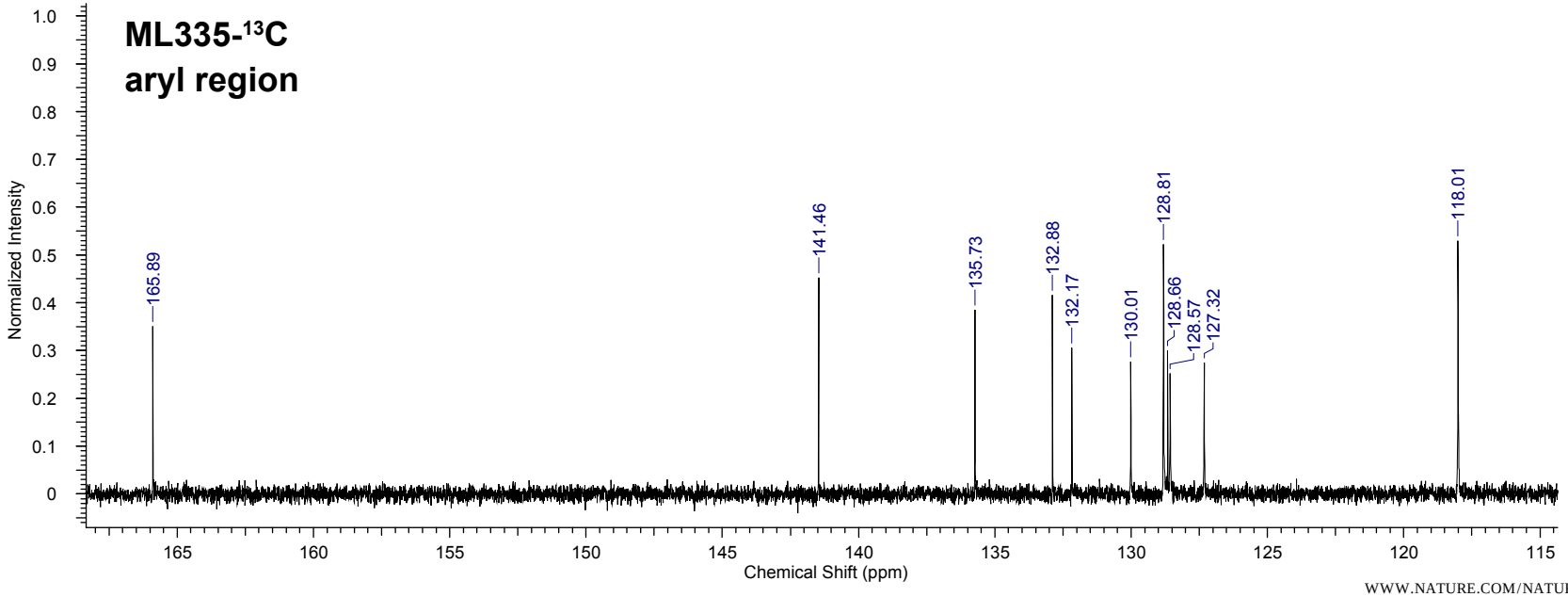
ML335-13C
aryl region
Normalized Intensity
Chemical Shift (ppm)
165.89
141.46
135.73
132.88
132.17
130.01
128.81
128.66
128.57
127.32
118.01

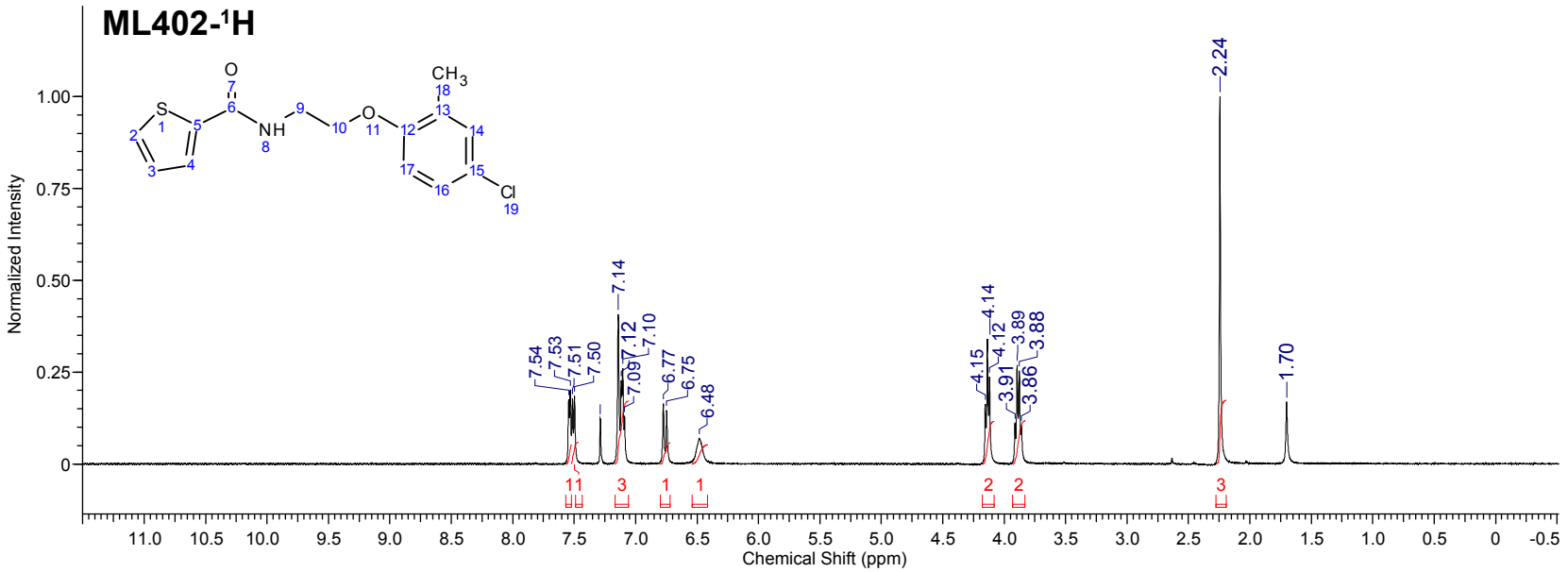
ML402-¹H
Normalized Intensity
Chemical Shift (ppm)
7.54
7.53
7.51
7.50
7.14
7.12
7.10
7.09
6.77
6.75
6.48
4.15
4.14
4.12
3.91
3.89
3.88
3.86
2.24
1.70
11
3
1
1
2
2
3

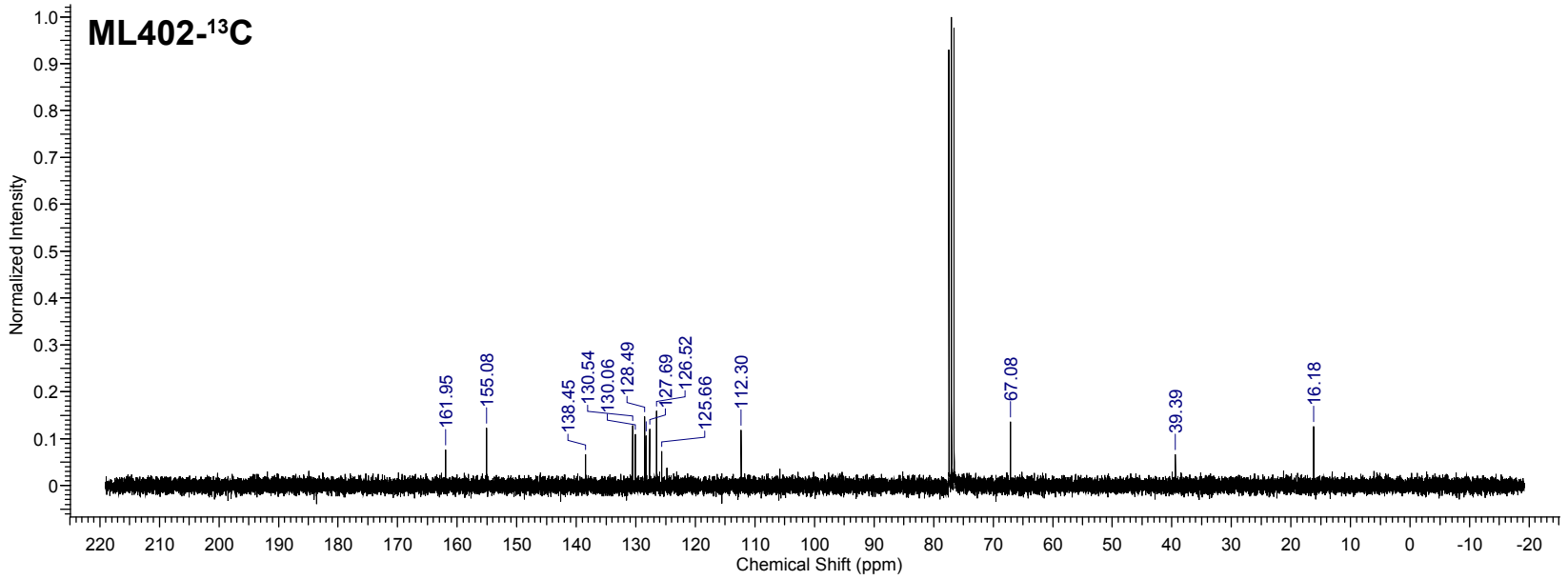
ML402-¹³C
Normalized Intensity
Chemical Shift (ppm)
161.95
155.08
138.45
130.54
130.06
128.49
127.69
126.52
125.66
112.30
67.08
39.39
16.18

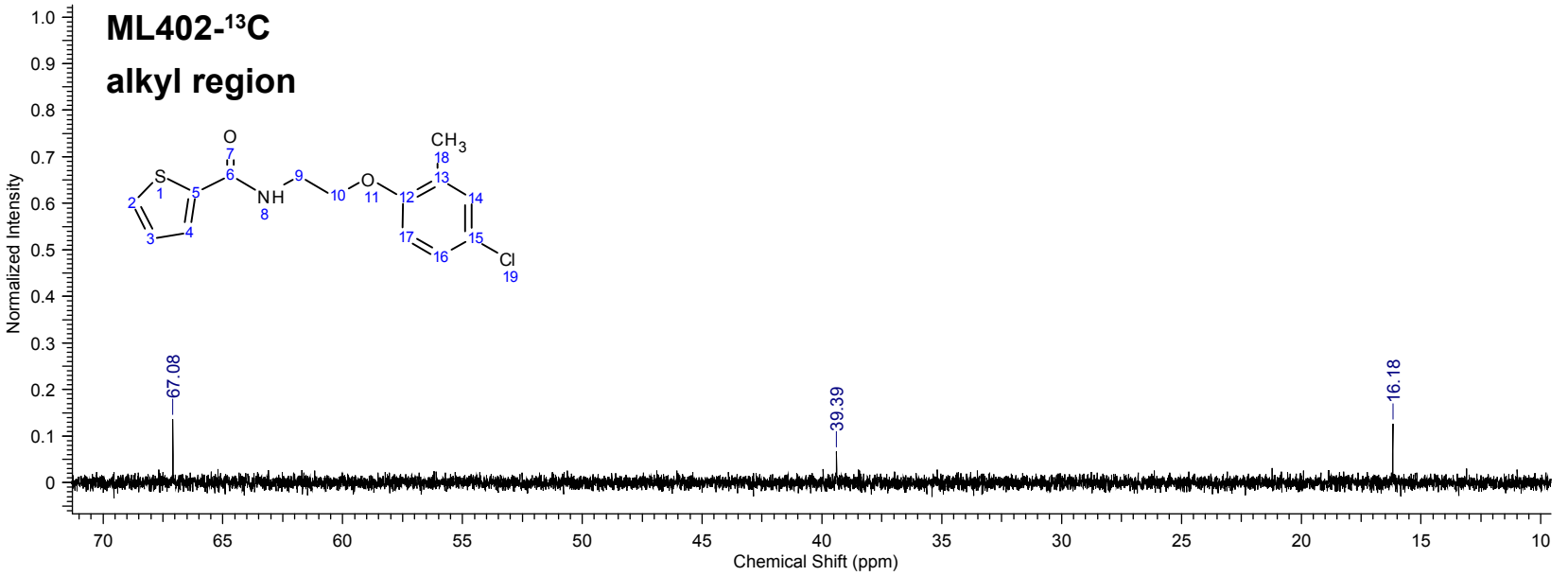
ML402-13C
alkyl region
Normalized Intensity
Chemical Shift (ppm)
67.08
39.39
16.18

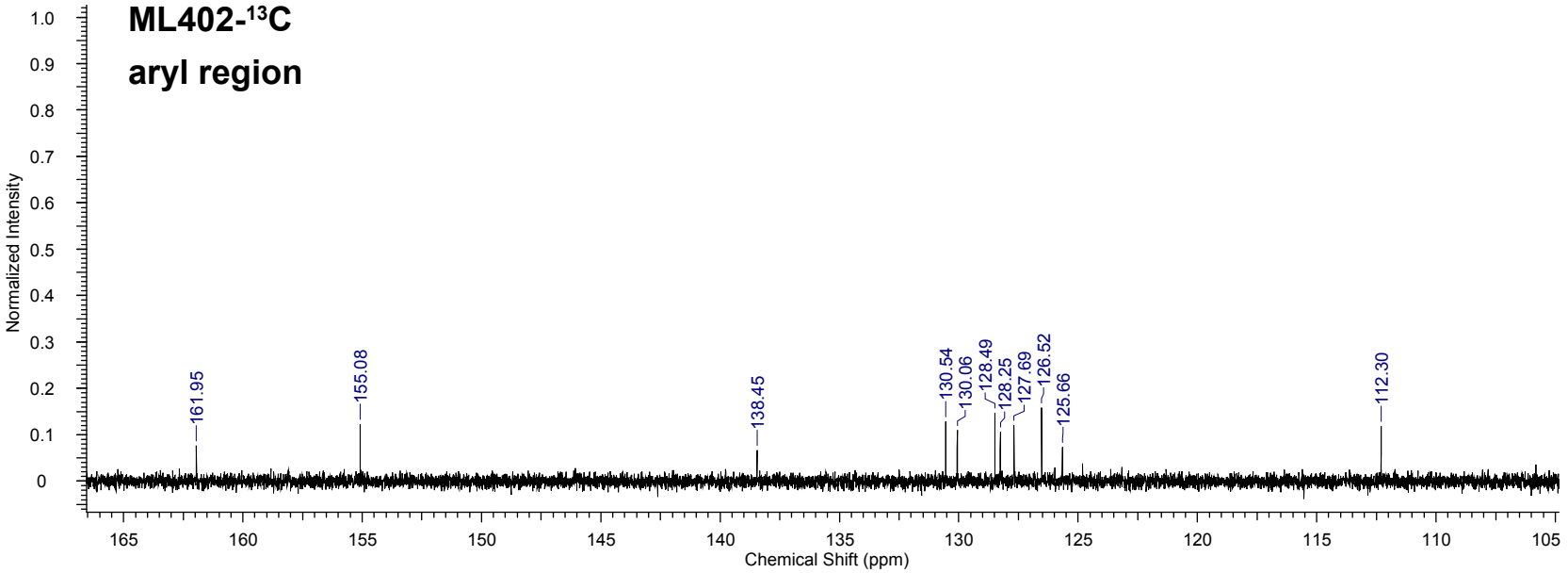
ML402-13C
aryl region
Normalized Intensity
Chemical Shift (ppm)
161.95
155.08
138.45
130.54
130.06
128.49
128.25
127.69
126.52
125.66
112.30

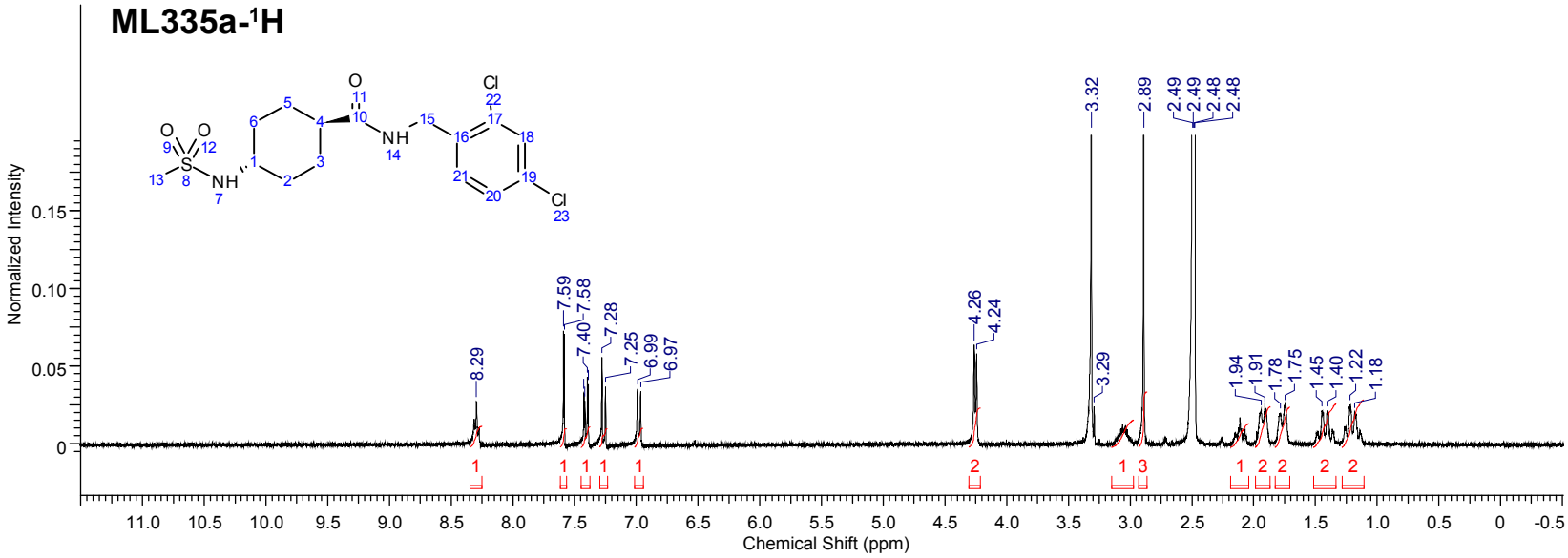
ML335a-1H
Normalized Intensity
Chemical Shift (ppm)
8.29
7.59
7.58
7.40
7.28
7.25
6.99
6.97
4.26
4.24
3.32
3.29
2.89
2.49
2.49
2.48
2.48
1.94
1.91
1.78
1.75
1.45
1.40
1.22
1.18

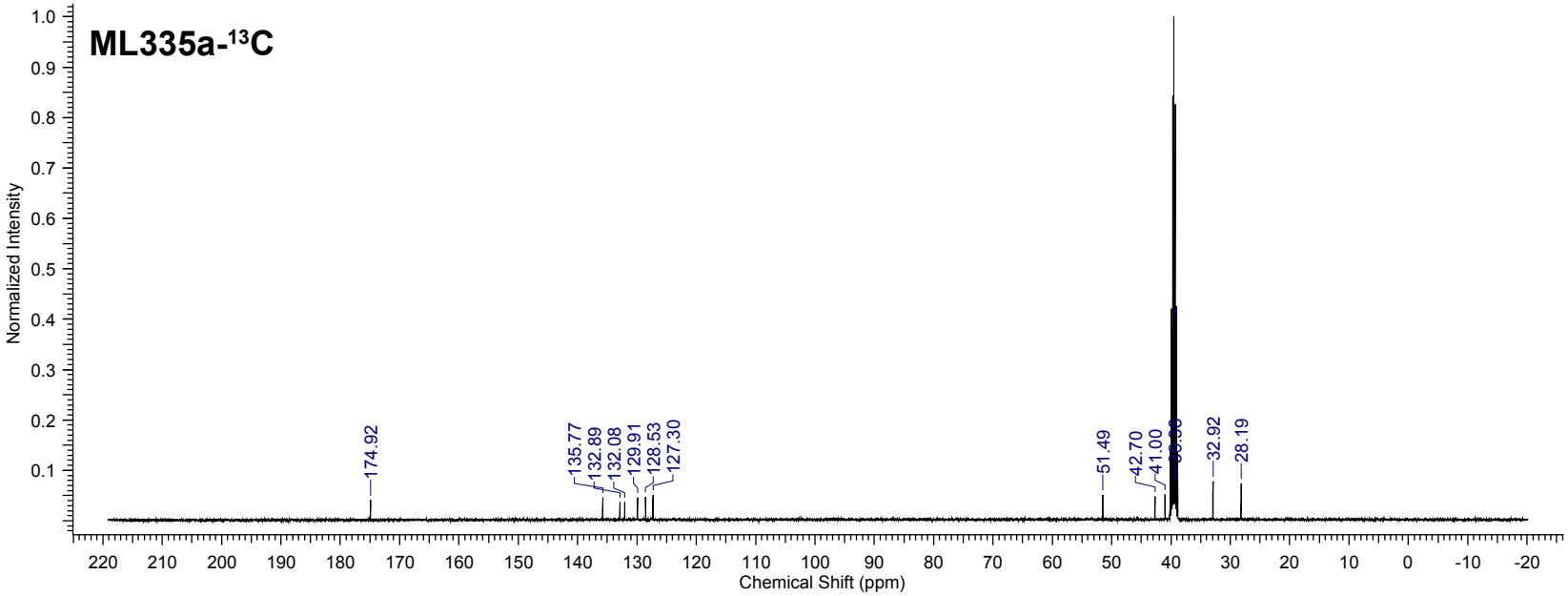
ML335a-13C
Normalized Intensity
Chemical Shift (ppm)
174.92
135.77
132.89
132.08
129.91
128.53
127.30
51.49
42.70
41.00
32.92
28.19

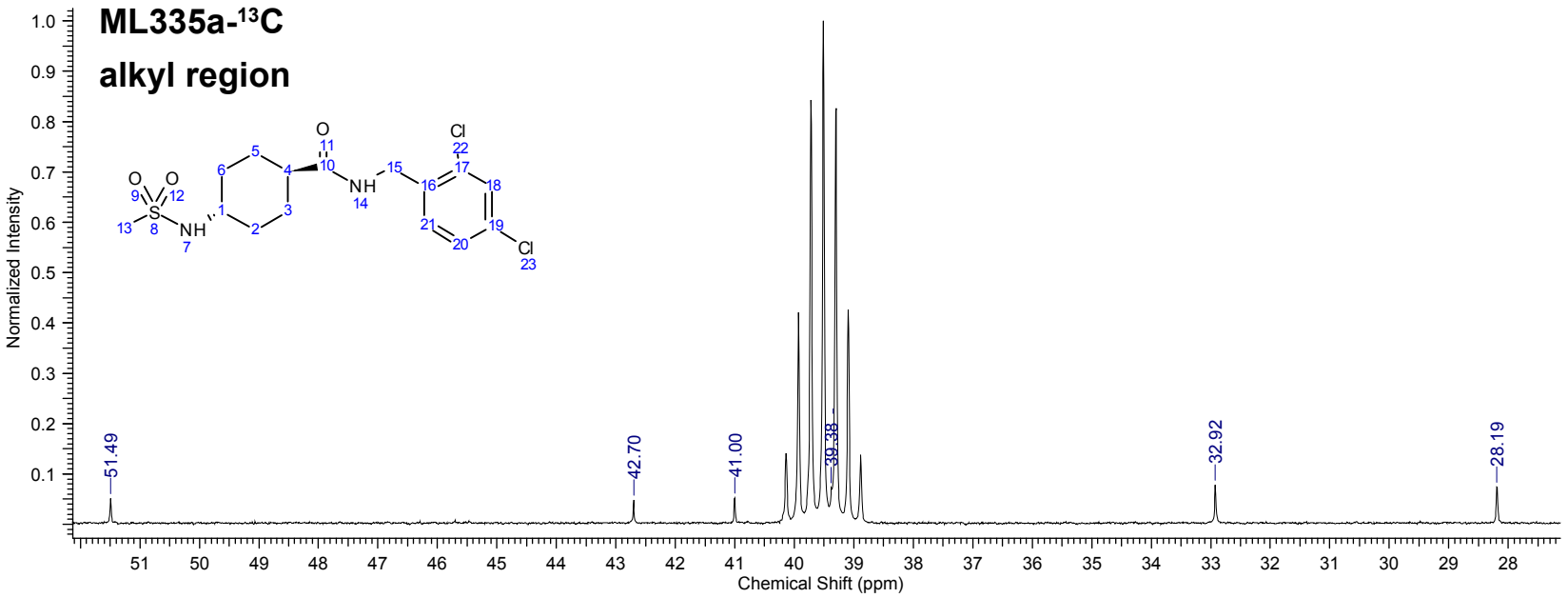
ML335a-13C
alkyl region
Normalized Intensity
Chemical Shift (ppm)
51.49
42.70
41.00
39.38
32.92
28.19

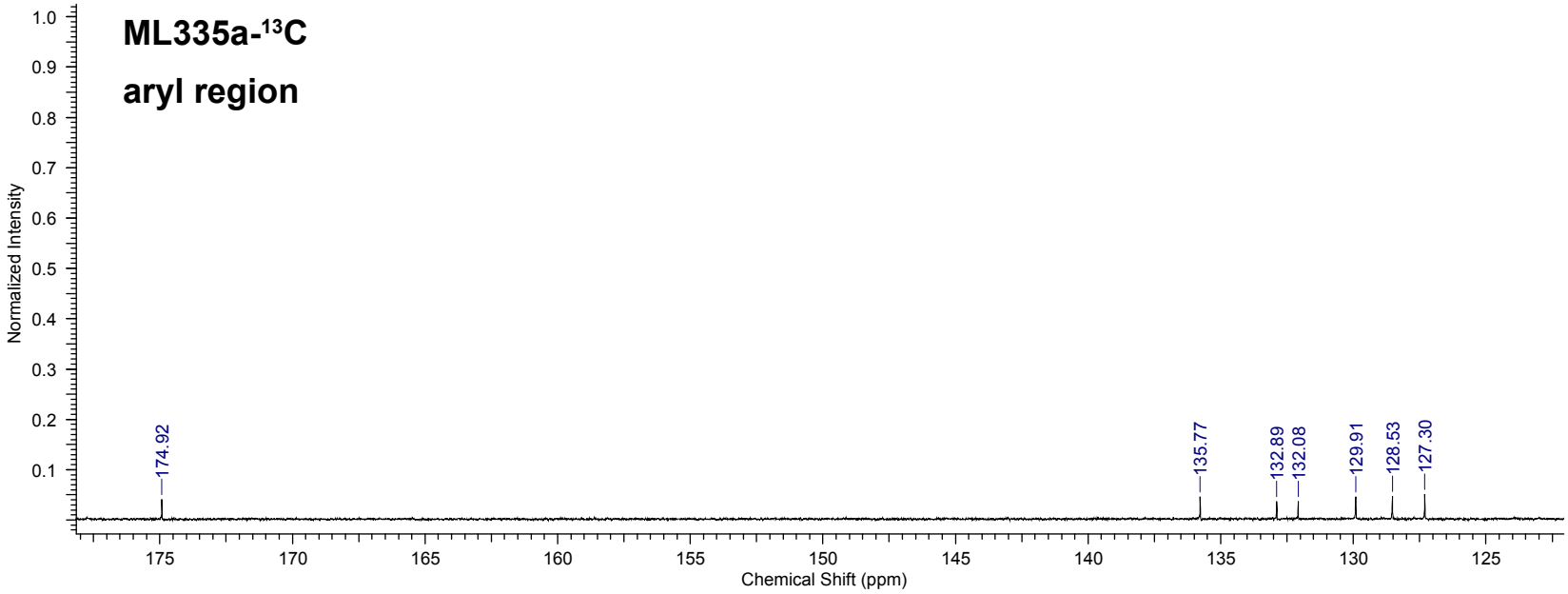
ML335a-13C
aryl region
Normalized Intensity
Chemical Shift (ppm)
174.92
135.77
132.89
132.08
129.91
128.53
127.30